nature communications

Article

https://doi.org/10.1038/s41467-025-62225-8

A genetically encoded biosensor for point-of-care and live-cell detection of D-2-hydroxyglutarate

Received: 5 February 2025

Accepted: 16 July 2025

Published online: 26 July 2025

Check for updates

Yidong Liu[1], Zhaoqi Kang[1], Rong Xu[1], Shuang Hou[1], Lingru Gong[1], Leilei Guo[1], Kaiyu Gao[1], Xianzhi Xu[1], Xiaoxu Tan[1], Dan Xiao[1], Wen Zhang[2], Gang Wang[3], Shaowu Ou[3], Jinqu Hu[3], Jiyuan Liu[3], Chuanjuan Lü[1], Cuiqing Ma[1], Ping Xu[4] & Chao Gao[1]

D-2-Hydroxyglutarate (D-2-HG) is a functional endogenous metabolite in various domains of life. Its abnormal accumulation promotes human tumorigenesis. Convenient D-2-HG testing for diagnosis and prognosis of D-2-HG-related diseases remains technically challenging, and there is no analytical method to directly detect D-2-HG in living cells. Here, we identify a D-2-HG-specific transcriptional activator, HgcR, and develop a D-2-HG sensor (DHOR) using HgcR as a sensing moiety. Then, we build a portable device adaptive with DHOR for rapid and low-cost point-of-care D-2-HG testing in serum, urine, and glioma tissue samples. DHOR also allow spatiotemporal resolution of D-2-HG in living bacteria and human cells. We use DHOR to identify D-2-HG transporters from *Escherichia coli* and human solute carrier 22 family. Overall, DHOR provides a powerful and versatile tool for in vitro and live-cell detection of D-2-HG, offering the opportunity to deepen our understanding about physiological and pathogenetic roles of D-2-HG.

Mutations in isocitrate dehydrogenase IDH1/2 of human cells result in neomorphic activity that catalyzes the reduction of 2-ketoglutarate (2-KG) to D-2-hydroxyglutarate (D-2-HG)[1,2]. Accumulation of D-2-HG and IDH mutation have been identified in a variety of cancers, including gliomas, acute myeloid leukemia, chondrosarcoma, etc[1]. D-2-Hydroxyglutaric aciduria (D2HGA), caused by D-2-hydroxyglutarate dehydrogenase (D2HGDH) or IDH mutations, also exhibits significantly elevated D-2-HG in the body fluids[3]. Thus, D-2-HG has emerged as a biomarker for the diagnosis and prognosis of IDH mutation-related cancers and D2HGA[3–6]. Conventional methods for detecting D-2-HG, such as liquid chromatography-tandem mass spectrometry (LC-MS/MS) and magnetic resonance spectroscopy (MRS), are time-consuming and incompatible with rapid point-of-care testing[7]. There is still an urgent need to develop a tool for cost-saving, rapid, and sensitive D-2-HG detection.

Massive accumulation of D-2-HG competitively inhibits the activity of various 2-KG-dependent dioxygenases, thereby promoting tumorigenesis and carcinogenesis via tumor cell-intrinsic epigenetic alterations[1]. In addition, overproduced D-2-HG in tumor cells with IDH mutations is released into the extracellular microenvironment and then taken up by T cells, impairing their anti-tumor functions[8,9]. Besides being a well-known oncometabolite, D-2-HG is also an endogenous metabolite involved in various metabolic processes, such as L-serine biosynthesis, 4-hydroxybutyrate degradation, and lysine catabolism[10]. Its concentration is maintained at a basal level by D2HGDH-catalyzed oxidation to 2-KG in normal cells[11]. A major

[1]State Key Laboratory of Microbial Technology, Shandong University, Qingdao, People's Republic of China. [2]Institute of Medical Sciences, The Second Hospital, Cheeloo College of Medicine, Shandong University, Jinan, People's Republic of China. [3]Department of Neurosurgery, The First Hospital of China Medical University, Shenyang, People's Republic of China. [4]State Key Laboratory of Microbial Metabolism, Joint International Research Laboratory of Metabolic & Developmental Sciences, and School of Life Sciences & Biotechnology, Shanghai Jiao Tong University, Shanghai, People's Republic of China. e-mail: jieerbu@sdu.edu.cn

challenge in deciphering the physiological and pathogenetic roles of the double-sided metabolite D-2-HG is the real-time measurement of its concentration and location in living cells.

Genetically encoded fluorescent sensors are effective tools for real-time monitoring of intracellular fluctuations of various metabolites[12–14]. Here, we find that *Pseudomonas putida* KT2440, a model environmental microbial strain, contains two D2HGDHs, PP5154 and PP4493. HgcR, a D-2-HG-specific transcriptional regulator, activates the transcription of *pp4493* in the presence of D-2-HG. Based on HgcR and circularly permutated yellow fluorescent protein (cpYFP), we develop a genetically encoded fluorescent sensor, DHOR, that produces a > 1700% ratiometric fluorescence increase to D-2-HG in vitro. Beyond a demonstration for point-of-care D-2-HG testing in serum, urine, and glioma samples, we show that DHOR also enables spatial and temporal resolution of D-2-HG in living cells. We use DHOR to analyze the effects of specific inhibitors on mutant IDH and the subcellular distribution of D-2-HG. In addition, we also use DHOR to identify the D-2-HG transporters in *Escherichia coli* and analyze the potential role of organic anion transporters (OATs) from the human solute carrier (SLC) 22 family in D-2-HG transport.

Results

Identification of HgcR as a D-2-HG-specific transcriptional activator

D-2-HG is oxidized to 2-KG by FAD-dependent D2HGDHs in most organisms[11,15]. Two types of D2HGDHs have been identified until now. D2HGDHs containing only the GlcD domain (FAD oxidoreductase domain) are widely distributed in microorganisms, plants, and animals[11]. D2HGDHs containing the GlcD and GlpC domains (Fe-S oxidoreductase domain) are mostly found in the *Proteobacteria* phylum[15]. Considering the cytotoxicity of D-2-HG, organisms need to sense D-2-HG and regulate the expression of D2HGDHs to prevent the excessive accumulation of D-2-HG[16]. We found that *P. putida* KT2440 has both two types of D2HGDHs, PP5154 and PP4493. PP5154 shares a high identity with reported D2HGDHs containing only the GlcD domain[11,17–19](Supplementary Fig. 1). PP4493, a putative FAD-dependent dehydrogenase that contains both GlcD and GlpC domains, has been previously shown to be involved in D-lysine catabolism in *P. putida* KT2440 by oxidizing D-2-HG to 2-KG[20] (Fig. 1a). Then, we identified the functions and regulatory mechanisms of these two D2HGDHs in *P. putida* KT2440.

Single knockout of gene *pp4493*, instead of gene *pp5154*, resulted in obvious growth defects of *P. putida* KT2440 with either D-2-HG or D-lysine as the sole carbon source (Fig. 1b–d and Supplementary Fig. 2). During the growth of *P. putida* KT2440(Δ*pp4493*) with D-lysine as the sole carbon source, extracellular D-2-HG accumulated until the logarithmic phase, but was thoroughly consumed with subsequent growth (Fig. 1e). These results suggest a predominant but not exclusive role for PP4493 in *P. putida* KT2440 D-2-HG catabolism. As expected, the knockout of both *pp5154* and *pp4493* completely abolished the ability of *P. putida* KT2440 to utilize D-2-HG or D-lysine (Fig. 1b, d). Thus, both PP5154 and PP4493 are active D2HGDHs involved in D-2-HG catabolism in *P. putida* KT2440. *P. putida* KT2440 is the only organism identified to have two types of D2HGDHs.

Then, we substituted the stop codons of genes *pp5154* or *pp4493* with gene *pGFPmut2* from plasmid pMRP9-1[21] to analyze the expression pattern of enzymes PP5154 and PP4493. Fluorescence intensities of *P. putida* KT2440(PP5154$_{GFP}$) were similar in the presence of glucose, D-2-HG, and L-2-HG, whereas only D-2-HG induced a significant increase in fluorescence intensity of *P. putida* KT2440(PP4493$_{GFP}$) (Fig. 1f). These results suggest that the expression of PP5154 is constitutive, whereas the expression of PP4493 is induced by D-2-HG. We noticed that the downstream gene of *pp4493*, gene *pp4494*, encodes a LysR-type transcriptional regulator (LTTR). The deletion of *pp4494* did not influence the growth of *P. putida* KT2440 in the presence of glucose but caused a significant defect in D-2-HG utilization (Fig. 1g, h). In addition, double knockout of *pp4494* and *pp5154* fully attenuated the ability of *P. putida* KT2440 to utilize D-2-HG (Fig. 1h). The gene *pp4493* expression was no longer induced by D-2-HG due to the *pp4494* deficiency (Fig. 1i), suggesting that PP4494 specifically senses D-2-HG and activates the *pp4493* expression. Thus, PP4494 was designated HgcR (D-2-hydroxyglutarate catabolic regulator).

Sodium dodecyl sulfate-polyacrylamide gel electrophoresis (SDS-PAGE) and gel filtration chromatography indicated that purified HgcR exists as a dimer in solution. The presence of D-2-HG did not change the oligomeric state of HgcR (Supplementary Fig. 3a, b). Electrophoretic mobility shift assays showed that HgcR bound to the promoter fragment of *pp4493* in a protein concentration-dependent manner (Fig. 1j). The migration distance of the HgcR-DNA complex was altered only by the addition of D-2-HG, rather than its analogs and metabolic precursors (Supplementary Fig. 3c). DNase I footprinting assays showed a distinct protected region of 48 bp when the DNA probe was incubated with HgcR, which shortened to 28 bp in the presence of D-2-HG (Fig. 1k). These results demonstrated that HgcR senses D-2-HG and activates the transcription of *pp4493* by directly interacting with its promoter. To sum up, D-2-HG is oxidized to 2-KG by both PP5154 and PP4493, and the transcription of *pp4493* is positively regulated by the D-2-HG-specific regulator HgcR (Fig. 1l).

Design and characterization of D-2-HG biosensor DHOR

HgcR exhibits high specificity for D-2-HG and is thus a promising sensing moiety for biosensor construction. We embedded a cpYFP between a pair of HgcR monomers or into the loop region between adjacent α-helice/β-strand of ligand-binding domain (LBD) of HgcR (Supplementary Fig. 4) to develop a series of single fluorescent protein-based D-2-HG fluorescent sensors (Fig. 2a and Supplementary Fig. 5). We evaluated the detection sensitivity of the insertion variants by analyzing their maximum fluorescence ratio changes (ΔR_{max}) in response to D-2-HG. The variant obtained by inserting cpYFP between 291 L and 292E of HgcR exhibited the highest ΔR_{max} of ~ 70% and was designated as DHOR$_{0.1}$ (Fig. 2b, c and Supplementary Fig. 6). To improve the sensitivity of the D-2-HG sensor, we generated a series of truncated variants of DHOR$_{0.1}$, and the best-performing variant (1–96 amino acids truncation, named DHOR$_{0.2}$) showed the highest ΔR_{max} of ~ 90% (Fig. 2a–c and Supplementary Fig. 7a–c).

We subsequently introduced four previously reported mutations[22] from the superfolder GFP into cpYFP (S30R, Y39N, N105T, and Y145F) to obtain DHOR$_{0.3}$, and the fluorescence intensity of DHOR$_{0.3}$ at 485 nm and 420 nm improved 376% and 69% compared to DHOR$_{0.2}$, respectively (Fig. 2a–c and Supplementary Fig. 7d–f). Finally, we combined random mutations at the N- and C-terminal linkers of DHOR$_{0.3}$ with high-throughput screening to further improve the dynamic range of the sensor (Fig. 2a and Supplementary Fig. 8). Seven mutants with high responses to D-2-HG were purified among 873 randomly selected mutants, and we found mutant #824 showed a relatively higher ΔR_{max} of ~ 1740% among the purified mutants and designated it as DHOR (Fig. 2a–c and Supplementary Fig. 9). Interestingly, the superfolder sites-introduced cpYFP (cpsfYFP) in DHOR is placed just three residues away from the C-terminus of HgcR. As shown in Supplementary Fig. 10, monomeric DHOR will undergo dimerization in the presence of D-2-HG. We predicted the structures of the monomeric and dimeric DHOR with AlphaFold3 (Fig. 2a). Subsequent molecular dynamics simulations indicated that dimeric D-2-HG-bound DHOR is more stable than D-2-HG-free monomer (Supplementary Fig. 11a). In addition, the dimerization of HgcR domain obviously altered the conformation of the tail region of DHOR and limited solvent access to the chromophore of cpsfYFP (Supplementary Fig. 11b–e), which may partially account for D-2-HG-induced fluorescence changes[23–25].

https://doi.org/10.1038/s41467-025-62225-8

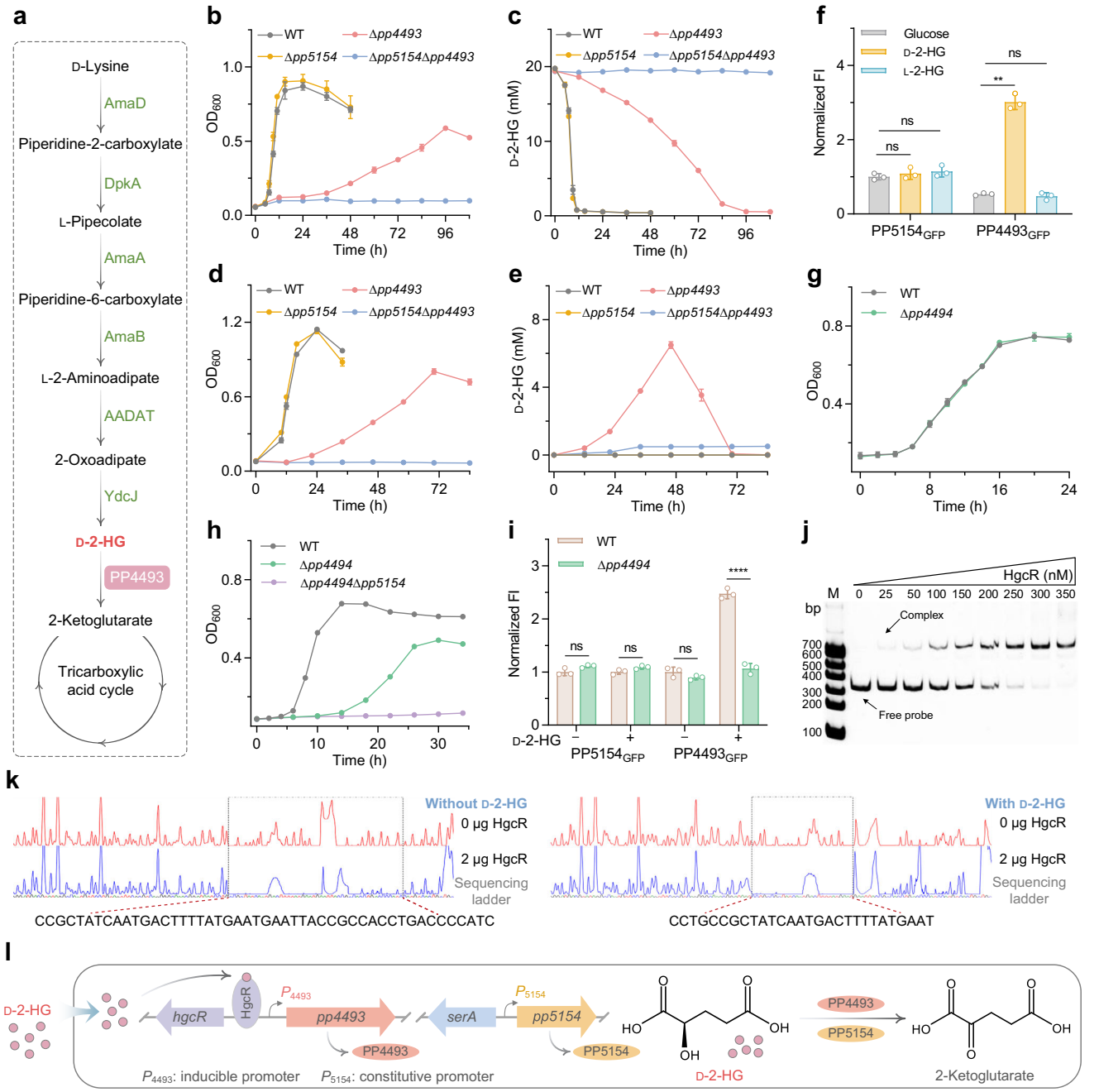

Fig. 1 | Identification of HgcR as a D-2-HG-specific activator. a D-Lysine metabolic pathways in *P. putida* KT2440. AmaD, D-lysine oxidase; DpkA, piperideine-2-carboxylate reductase; AmaA, L-pipecolate oxidase; AmaB, piperidine-6-carboxylate dehydrogenase; AADAT, aminoadipate aminotransferase; YdcJ, 2-hydroxyglutarate synthase. **b**, **c** *P. putida* KT2440 wild-type (WT) and its derivatives were grown with 20 mM D-2-HG as the sole carbon source. The growth (**b**) and D-2-HG consumption (**c**) were measured. **d**, **e** *P. putida* KT2440 and its derivatives were grown with 20 mM D-lysine as the sole carbon source. The growth (**d**) and D-2-HG concentration (**e**) were measured. **f** Expression of PP5154 and PP4493 at stationary growth phase of *P. putida* KT2440 with 5 g L^{-1} glucose, D-2-HG, or L-2-HG as the carbon source. Fluorescence intensities (FI) were divided by optical density at 600 nm (OD_{600}) and normalized to the glucose group value of $PP5154_{GFP}$. Two-tailed Student's *t* tests, $PP4493_{GFP}$: $P = 1.9 \times 10^{-3}$ for L-2-HG vs. D-2-HG. **g**, **h** The growth of *P. putida* KT2440 and its derivatives with 20 mM glucose (**g**) or D-2-HG (**h**) as the sole carbon source. **i** Expression of PP5154 and PP4493 at stationary growth phase of *P. putida* KT2440 or *P. putida* KT2440(Δ*pp4494*). 2.5 g L^{-1} glucose with or without 2.5 g L^{-1} D-2-HG were used as the carbon source. Data were divided by OD_{600} and normalized by the respective values of WT in glucose. $PP4493_{GFP}$ with D-2-HG: $P = 5.9 \times 10^{-5}$ for WT vs. Δ*pp4494*. **j** HgcR can bind to the promoter region of *pp4493*. Lane M, DNA molecular weight markers. **k** DNase I footprinting analysis of HgcR binding to the *pp4493* promoter region in the absence or presence of 20 mM D-2-HG. The regions protected by HgcR are boxed. **l** Schematic of D-2-HG metabolic regulation in *P. putida* KT2440. PP5154 and PP4493 catalyze the oxidation of D-2-HG to 2-KG. HgcR recognizes D-2-HG and activates the transcription of *pp4493*. All data shown are means ± standard deviations (SD) ($n = 3$ biological replicates) (**b**–**i**). ns, no significant difference ($P \geq 0.05$); $^{**}P < 0.01$; $^{****}P < 0.0001$. Source data are provided as a Source Data file.

DHOR exhibited an apparent dissociation constant (K_d) value ~ 940 μM, and a limit of detection (LOD) of ~ 2 μM toward D-2-HG (Fig. 2b). It has two excitation maxima at 416 nm and 502 nm, and the corresponding peak emission wavelengths are both approximately 515 nm (Fig. 2d, e). The presence of 1 mM D-2-HG induced a 51% increase and an 85% decrease in the fluorescence intensity at 420 nm and 485 nm excitation, respectively (Fig. 2e). The extinction coefficients, quantum yields, and brightness of DHOR in the presence and

https://doi.org/10.1038/s41467-025-62225-8

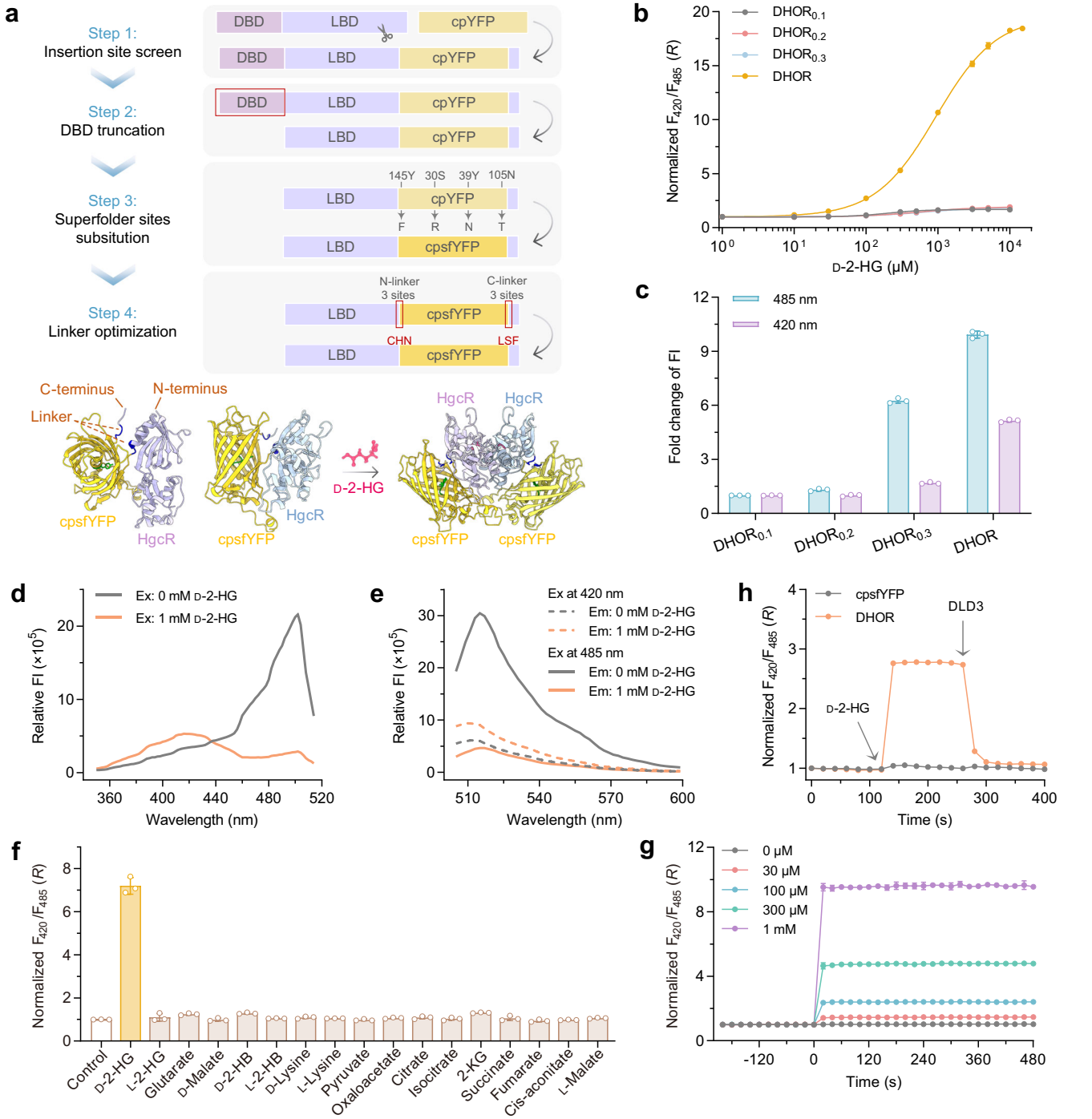

Fig. 2 | Design and characterization of D-2-HG sensor DHOR. a Schematic diagram of the construction and optimization of DHOR (D-2-HG sensor). DBD, DNA-binding domain; LBD, ligand-binding domain. Structures of monomeric and dimeric DHOR were predicted by AlphaFold3. Molecular docking of D-2-HG into the dimer was performed by Meastro. The HgcR domain is shown in purple and light blue. The cpsfYFP domain is shown in yellow. Linker is shown in blue. The chromophore of cpsfYFP is displayed as green sticks. **b**, **c** Dose-response curves (**b**) and fluorescence intensities (FI) (**c**) comparison of $DHOR_{0.1}$, $DHOR_{0.2}$, $DHOR_{0.3}$, and DHOR. Data were normalized to the initial value (**b**) and to the value of $DHOR_{0.1}$ (**c**). **d**, **e** DHOR excitation spectrum scan with 530 nm emission (**d**) and emission spectrum scan with 420 nm and 485 nm excitation (**e**) in the presence or absence of 1 mM D-2-HG. **f** Specificity analysis of DHOR. Fluorescence responses of DHOR to 500 μM indicated compounds. D-2-HB, D-2-hydroxybutyrate; L-2-HB, L-2-hydroxybutyrate. Data were normalized to the control group, in which an equal volume of ddH_2O was added to the system instead of any compound. **g** Kinetics of fluorescence response of DHOR to D-2-HG. Data were normalized to the initial value of 0 μM. **h** Reversibility analysis of DHOR. 200 μM D-2-HG and 0.05 mg mL^{-1} D-2-HG transhydrogenase DLD3 from *S. cerevisiae* S288C were sequentially added to the assay system previously containing 2 μM DHOR (or cpsfYFP) and 4 mM pyruvate. Data were normalized to the initial value. Data shown are means ± SD ($n = 3$ technical replicates in **b**, **c**, **f** and $n = 3$ biological replicates in **g**). Source data are provided as a Source Data file.

absence of D-2-HG were also measured (Supplementary Table 1). Its highest quantum yield (0.58) is close to that of enhanced GFP (EGFP, 0.60). DHOR was highly specific for D-2-HG, displaying no apparent fluorescence ratio change toward or in the presence of D-2-HG structural analogs, metabolic precursors, or tricarboxylic acid cycle intermediates (Fig. 2f and Supplementary Fig. 12a), and the presence of L-2-HG or 2-KG did not affect the dose-response curve of DHOR toward D-2-HG (Supplementary Fig. 12b). DHOR slightly responded to D-lactate or L-lactate at concentrations higher than 10 mM (Supplementary Fig. 12c). Since the lactate concentrations in serum or tumor environment can arise to tens of millimoles after strenuous exercise or under specific pathological states[26–29], the interfere of lactate toward D-2-HG detection with DHOR may need to be taken into account when necessary. The fluorescence ratios of DHOR reached a stable value within 20 s after D-2-HG addition (Fig. 2g), indicating the rapid response of the sensor. In addition, the response of DHOR remained stable between 20 and 37 °C (Supplementary Fig. 12d). Like other circularly permuted fluorescent protein-based sensors[22,30], the response of DHOR to D-2-HG was pH sensitive (Supplementary Fig. 12e, f). Therefore, we used cpsfYFP, which has similar pH sensitivity to DHOR (Supplementary Fig. 12g), to correct for pH effects[22,30]. The corrected fluorescence ratios of DHOR remained stable between pH 6.6 and 8.2 (Supplementary Fig. 12h). To analyze the reversibility of DHOR, D-2-HG and D2HGDH from *Saccharomyces cerevisiae* (DLD3)[19] were sequentially added to the detection system. We observed an elevated fluorescence ratio of DHOR induced by D-2-HG addition and a decreased ratio induced by DLD3-mediated D-2-HG consumption, whereas the ratio of cpsfYFP was not affected throughout the process (Fig. 2h). Taken together, DHOR showed high responsiveness, wide detection range, and good selectivity, making it a promising tool for D-2-HG detection in vitro and in vivo.

Portable fluorescence detector for point-of-care D-2-HG testing

Prior to exploring the in vivo application of DHOR, we sought to assess its application potential in clinical diagnostics. D-2-HG concentrations in body fluids are increased in patients with D-2-hydroxyglutaric aciduria and with IDH mutation-related cancers like acute myeloid leukemia, gliomas, and breast carcinoma[3,6,31,32]. The detection of D-2-HG in body fluids is thus relevant for the diagnosis and prognostic assessment of D-2-HG-related diseases. In addition, glioma is a prevalent brain cancer with poor 5-year survival rates[33]. In the 2021 World Health Organization classification of tumors of the central nervous system, IDH mutation status has been included in the diagnosis criteria of glioma (both intraoperatively and postoperatively)[33,34]. D-2-HG, which is produced from 2-KG by mutant IDH, is a reliable surrogate indicator for IDH mutation status[34,35].

However, D-2-HG quantification by DHOR with a fluorescent microplate reader is incompatible with convenient and cost-saving point-of-care D-2-HG testing. Thus, we designed a simple fluorescence detection device for point-of-care D-2-HG detection with DHOR (Fig. 3a). Briefly, the sample to be detected is mixed with DHOR and excited using two light-emitting diodes (LEDs) with emission wavelengths at 415 nm and 475 nm, respectively. The emission spectra are collected using an integrating sphere, which can enhance both excitation and collection efficiencies through repeatedly reflecting the incident and emitted light with the diffuse reflective coating. We built the prototype device using inexpensive off-the-shelf optics and electronics (Fig. 3b). A disposable PCR tube in a 3D printed sample holder is used as a cuvette for D-2-HG detection. A charge-coupled device spectrometer is connected to a laptop with a fiber optic to output detection results. To evaluate the performance of this device coupled to DHOR for detecting D-2-HG, serial dilutions of D-2-HG in potassium phosphate buffer were used to produce a dose-response curve. The presence of D-2-HG did not affect the fluorescence intensity at 415 nm but obviously decreased the intensity at 475 nm (Supplementary Fig. 13). DHOR can still generate a usable dose-response curve toward D-2-HG with a ΔR_{max} of ~380% using the proof-of-concept device (Fig. 3c). Since this proof-of-concept device used an LED light source and a charge-coupled device spectrometer with no signal amplification function, the decreases in fluorescence intensity at 475 nm could not be monitored when D-2-HG concentration increased above 3 mM (Supplementary Fig. 13). Compared with those obtained with a fluorescence microplate reader, the dose-response curve of DHOR detected by the device reached a plateau at a lower D-2-HG concentration and the K_d decreased to ~210 μM (Fig. 3c).

To explore the applicability of DHOR for quantifying D-2-HG in human body fluids by using the prototype device, we spiked various concentrations of D-2-HG into healthy human serum and urine to simulate clinical samples (Fig. 3d). For each test, 15 μL of serum or urine was mixed with 45 μL of DHOR diluted in potassium phosphate buffer and detected using the prototype device. To validate the quantification results of DHOR, the same samples were also measured by the standard laboratory method, LC-MS/MS, in parallel. D-2-HG concentrations of serum and urine samples quantified by DHOR were in good agreement with LC-MS/MS (Fig. 3e–h), indicating the accuracy of DHOR and the usability of the device for D-2-HG measurement.

Subsequently, we evaluated the capability of DHOR with the device to detect D-2-HG in tumor tissue, first using mouse tumors as test objects. Human glioblastoma U87MG cells with wild-type IDH1 or R132H-mutant IDH1 ($IDH1^{R132H}$) were subcutaneously inoculated into the flanks of nude mice to induce tumor formation, and the tumors were removed after 31 days. Approximately 100 mg of tumor tissue from each sample was homogenized in 400 μL of potassium phosphate buffer using a hand grinder. The tissue homogenates were centrifuged, and the supernatants were filtered before mixed with DHOR (Fig. 3i). As detected by the device, D-2-HG levels were significantly higher in tumors with $IDH1^{R132H}$ (2.583 μmol g^{-1}) than in those with wild-type IDH1 (0.085 μmol g^{-1}) (Fig. 3j). A Bland-Altman analysis suggested that the D-2-HG concentrations in IDH-mutant tumor tissues quantified by the prototype device showed good agreement with the results obtained by LC-MS/MS (Fig. 3k).

We also collected resected glioma tissues from 21 patients and processed these tissues using the same procedure as for the mouse tumors and performed D-2-HG quantification with the prototype device (Fig. 3i). The average D-2-HG level (2.278 μmol g^{-1}) of 10 samples harboring mutant IDH was apparently higher than that (0.095 μmol g^{-1}) of 11 samples with wild-type IDH, although the individual D-2-HG concentration varied widely in clinical IDH-mutant gliomas (0.481–4.742 μmol g^{-1}) (Fig. 3l). This demonstrates that the prototype device-based D-2-HG detection method can distinguish the gliomas with mutant IDH from the wild-type. The data obtained using the device showed high consistency with LC-MS/MS-based D-2-HG quantitation (Fig. 3m). In addition, given that the tumor tissue sample processing and fluorescence analysis with the prototype device allowed rapid D-2-HG measurement within approximately 5 min, these findings support the potential application of DHOR for intraoperative diagnosis of IDH mutation status.

Characterization of D-2-HG metabolism and transport in *E. coli*

Next, we explored the utility of DHOR for detecting D-2-HG in living bacteria. When expressed in *E. coli* type strain W3110(DE3), DHOR exhibited an immediate, dose-dependent increase in the fluorescence ratio in response to the addition of exogenous D-2-HG, demonstrating the applicability of DHOR in living bacteria (Fig. 4a, b). *E. coli* has only one D2HGDH, named YdiJ[15], which has both GlcD and GlpC domains and shares 51.10% identity with PP4493 (Fig. 4c, d). To further validate the performance of DHOR for detecting endogenous D-2-HG variation in *E. coli*, we knocked out the entire *ydiJ* gene or its GlcD/GlpC domain in *E. coli* W3110(DE3). DHOR was expressed in mutant strains to analyze intracellular D-2-HG levels. Knockout of *ydiJ* or any of its domains

https://doi.org/10.1038/s41467-025-62225-8

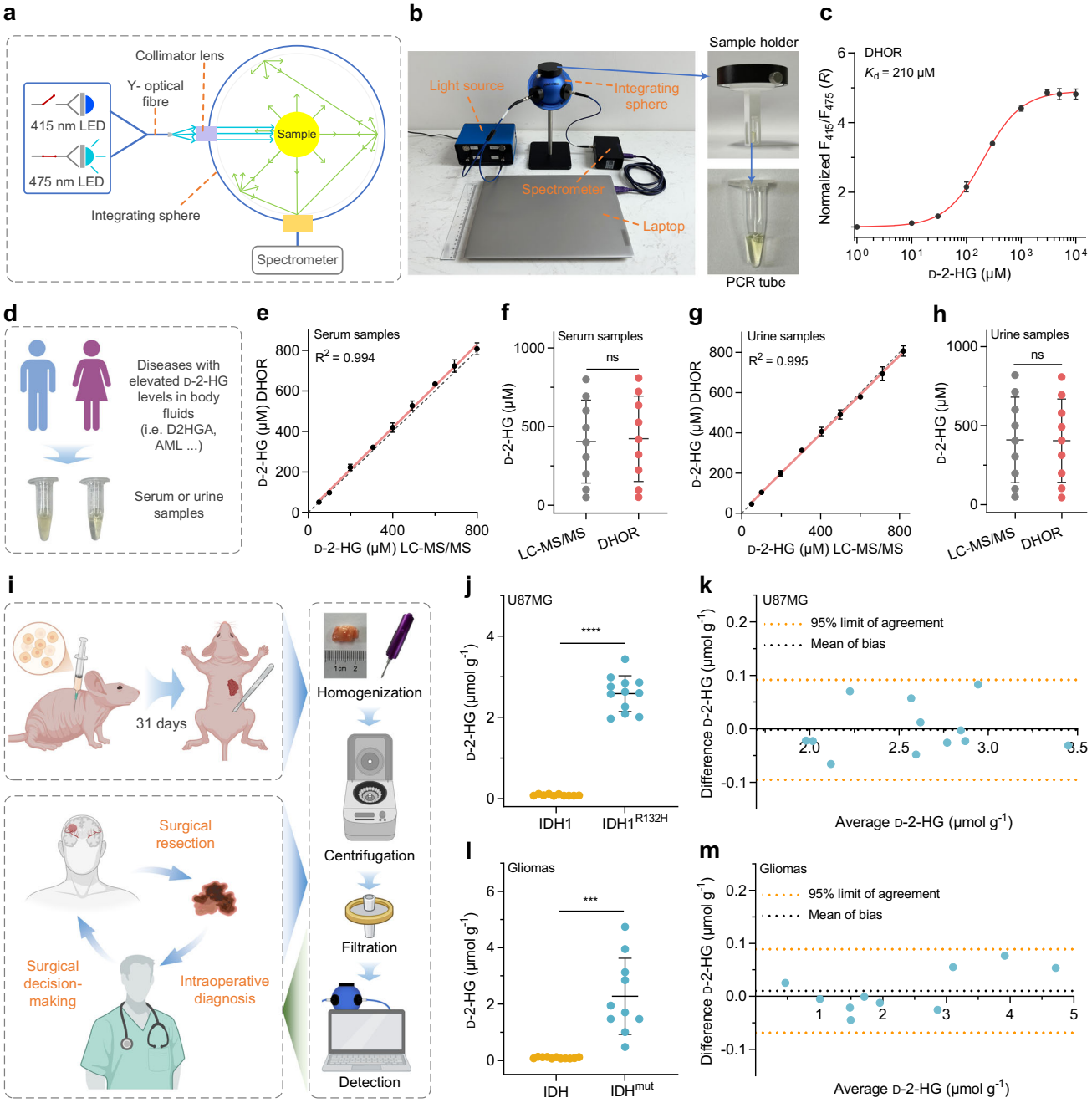

Fig. 3 | Portable fluorescence detector for point-of-care D-2-HG testing. a, **b** Schematic diagram (**a**) and a photograph (**b**) of the prototype device. The sample is excited by a 475 nm or 415 nm LED. The emitted light is diffusely reflected by the integrating sphere and collected by the spectrometer adapted to the laptop. **c** Dose-response curve obtained by the prototype device for D-2-HG detection. Data were normalized to the initial value ($n = 3$ technical replicates). **d**–**h** Application of the prototype device in quantification of D-2-HG in human body fluid samples. Examples of body fluid samples associated with D-2-HG-related diseases, such as D-2-hydroxyglutaric aciduria (D2HGA) and acute myeloid leukemia (AML) with D2HGDH or IDH mutation (**d**). Comparison between the quantitative results of D-2-HG in serum (**e**, **f**) and urine (**g**, **h**) obtained by the prototype device and LC-MS/MS. Gray dotted line indicated a reference line with slope of 1 ($n = 3$ technical replicates in **e**, **g** and $n = 9$ biological replicates in **f**, **h**). **i** General overview of the procedure for D-2-HG assay in resected mouse tumors and gliomas. **j** Comparison of D-2-HG levels in mouse tumors originated by subcutaneous inoculation of U87MG cells with wild-type IDH1 ($n = 10$ samples) or R132H-mutant IDH1 ($n = 12$ samples). Two-tailed Student's t tests, $P = 5.9 \times 10^{-10}$. **k** Bland-Altman analysis for D-2-HG in IDH1^{R132H}-mutant mouse tumor samples measured by the prototype device and LC-MS/MS. Bias (black dotted line) and 95% limits of agreement (yellow dotted lines) were shown. **l** Comparison of D-2-HG levels in resection tissue samples from human glioma with wild-type IDH ($n = 11$ samples) or mutant IDH ($n = 10$ samples). $P = 6.4 \times 10^{-4}$. **m** Bland-Altman analysis for D-2-HG in IDH1-mutant glioma tissue samples measured by the prototype device and LC-MS/MS. Bias (black dotted line) and 95% limits of agreement (yellow dotted lines) were shown. Data shown are means ± SD (**c**, **e**–**h**, **j**, **l**). ns, no significant difference ($P \geq 0.05$); ***$P < 0.001$; ****$P < 0.0001$. Some elements of this figure were created in BioRender. Liu, Y. (2025) https://BioRender.com/zz1zft1. Source data are provided as a Source Data file.

https://doi.org/10.1038/s41467-025-62225-8

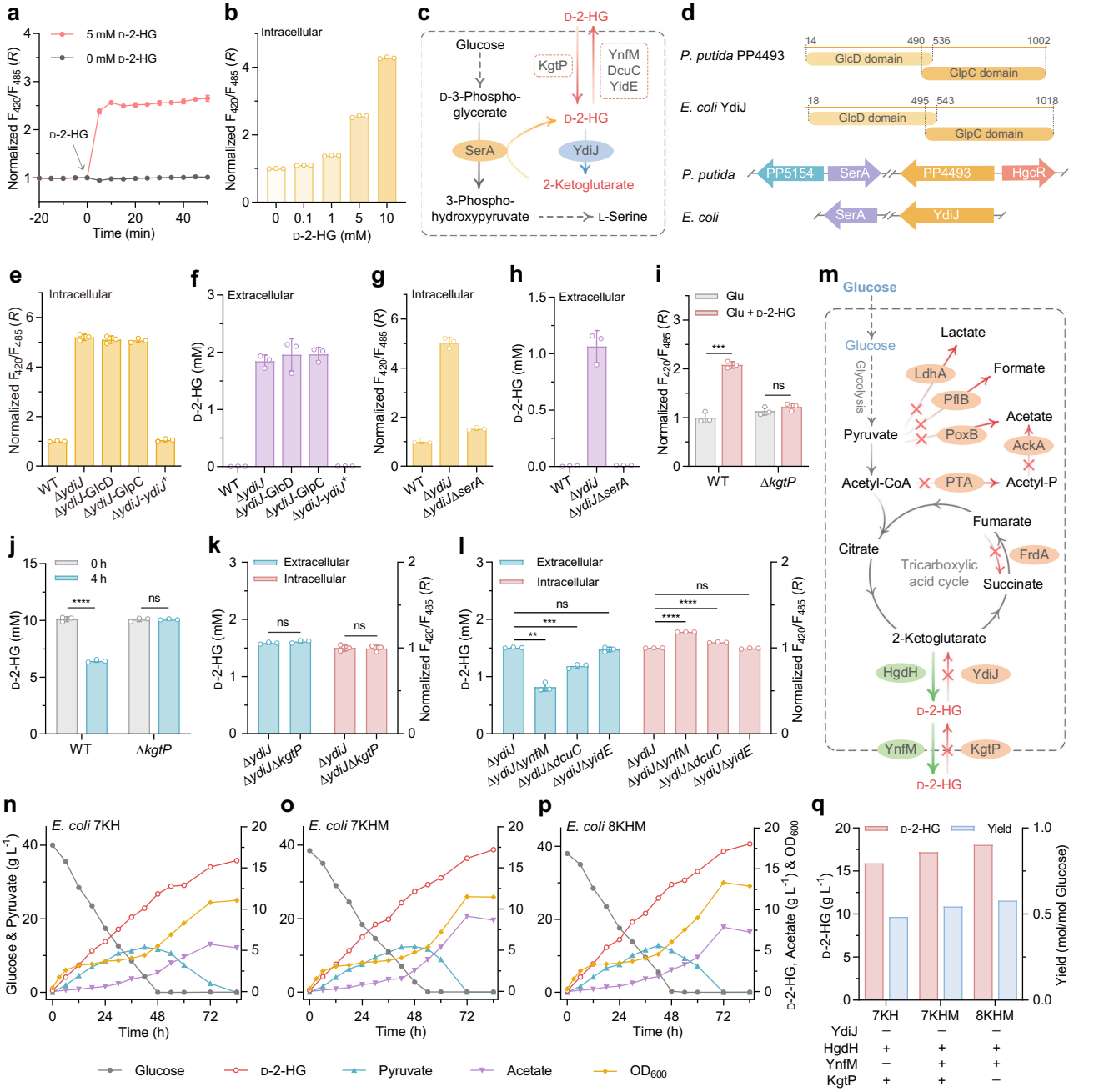

Fig. 4 | Characterization of D-2-HG metabolism and transport in *E. coli* to promote D-2-HG manufacture. a Kinetics of DHOR expressed in *E. coli* W3110(DE3) in response to 5 mM D-2-HG addition. Data were normalized to the values at time 0. **b** Fluorescence responses of DHOR expressed in *E. coli* W3110(DE3) to different concentrations of D-2-HG. Data were normalized to the value of 0 mM D-2-HG. **c** Schematic diagram of D-2-HG metabolic and transport mechanisms in *E. coli*. **d** Domain analysis and gene arrangement of PP4493 and YdiJ. **e**–**h** Identification of the metabolic mechanism of D-2-HG in *E. coli*. Fluorescence ratios of DHOR expressed in *E. coli* W3110(DE3) wild-type (WT) and its derivatives with 10 mM glucose as the carbon source (**e**, **g**). Data were normalized to the value of the WT group (**e**, **g**). Extracellular D-2-HG accumulation at 14 h when *E. coli* W3110(DE3) and its derivatives were grown with 25 mM glucose (**f**) or 25 mM glucose and 4 mM L-serine (**h**) as the carbon source. *ydiJ**, *ydiJ* complement. **i**, **j** D-2-HG uptake function analysis of KgtP. Fluorescence ratios of DHOR expressed in *E. coli* W3110(DE3) and its derivatives with 10 mM glucose (Glu) or with 10 mM glucose and 10 mM D-2-HG (Glu + D-2-HG) as the carbon source (**i**). Data were normalized to the Glu group value of WT (**i**). Extracellular D-2-HG concentration of *E. coli* W3110(DE3) and its derivatives after cultivating for 4 h with 10 mM glucose as the carbon source at OD_{600} of 5 (**j**). Two-tailed Student's *t* tests, WT: $P = 1.2 \times 10^{-4}$ for Glu vs. Glu + D-2-HG (**i**). WT: $P = 1.1 \times 10^{-5}$ for 0 h vs. 4 h (**j**). **k**, **l** D-2-HG efflux function analysis of KgtP, YnfM, DcuC, and YidE (homolog of SucE). Extracellular D-2-HG concentrations of *E. coli* W3110(DE3) and its derivatives were measured after cultivating for 24 h with 10 mM glucose as the carbon source at an OD_{600} of 5. Fluorescence ratios of DHOR expressed in *E. coli* W3110(DE3) and its derivatives were measured with 10 mM glucose as the carbon source. Fluorescence ratios were normalized to the value of the Δ*ydiJ* group. Extracellular: $P = 3.4 \times 10^{-3}$ for Δ*ydiJ* vs. Δ*ydiJ*Δ*ynfM*, $P = 1.5 \times 10^{-4}$ for Δ*ydiJ* vs. Δ*ydiJ*Δ*dcuC*; Intracellular: $P = 6.1 \times 10^{-9}$ for Δ*ydiJ* vs. Δ*ydiJ*Δ*ynfM*, $P = 2.9 \times 10^{-5}$ for Δ*ydiJ* vs. Δ*ydiJ*Δ*dcuC* (**l**). **m** Engineering strategies employed for D-2-HG production from glucose in *E. coli* BL21(DE3). LdhA, lactate dehydrogenase A; PflB, pyruvate-formate lyase; PoxB, pyruvate oxidase; PTA, phosphotransacetylase; AckA, acetate kinase A; FrdA, fumarate reductase subunit A; YdiJ, D-2-HG dehydrogenase; KgtP, 2-KG permease; HgdH, NAD^+-dependent D-2-HG dehydrogenase; YnfM, dicarboxylate transporter. **n**–**p** Time course of D-2-HG production by *E. coli* 7KH, *E. coli* 7KHM, and *E. coli* 8KHM. **q** Comparison of the production and yield of D-2-HG produced by *E. coli* 7KH, *E. coli* 7KHM, and *E. coli* 8KHM. Data shown are means ± SD ($n = 3$ biological replicates) (**a**, **b**, **e**–**l**). ns, no significant difference ($P \geq 0.05$); $^{**}P < 0.01$; $^{***}P < 0.001$; $^{****}P < 0.0001$. Source data are provided as a Source Data file.

resulted in intracellular D-2-HG accumulation to the same extent (Fig. 4e), indicating that GlcD and GlpC domains are both indispensable for D-2-HG dehydrogenation activity of YdiJ. We also used DHOR to detect extracellular D-2-HG of these strains and obtained similar results as with intracellular (Fig. 4f), further confirming the reliability of DHOR to characterize D-2-HG levels in living bacteria.

D-3-Phosphoglycerate dehydrogenase (SerA) catalyzes the initial step for L-serine synthesis. It is a transhydrogenase that catalyzes hydrogen transfer between 2-KG and D-3-phosphoglycerate, generating D-2-HG and 3-phosphohydroxypyruvate as end products[11,36] (Fig. 4c). To verify the role of SerA in D-2-HG production in *E. coli*, we knocked out *serA* in *E. coli* W3110(DE3)(Δ*ydiJ*). DHOR was also used to detect both intracellular and extracellular D-2-HG. The deletion of *serA* inhibited the D-2-HG accumulation caused by *ydiJ* knockout (Fig. 4g, h), supporting that SerA and YdiJ are the enzymes responsible for the generation and degradation of D-2-HG in *E. coli*, respectively (Fig. 4c).

KgtP, a major facilitator superfamily transporter, is required for the uptake of 2-KG by *E. coli*[37]. Considering the structural similarity between D-2-HG and 2-KG[2], KgtP may also participate in the uptake of D-2-HG by *E. coli*. When expressed in *E. coli* W3110(DE3)(Δ*kgtP*), DHOR did not respond to the addition of exogenous D-2-HG (Fig. 4i). The added D-2-HG was also not consumed (Fig. 4j), indicating that KgtP is apparently the D-2-HG importer in *E. coli*. In addition, when *kgtP* was knocked out in *E. coli* W3110(DE3)(Δ*ydiJ*), the fluorescence ratio of intracellularly expressed DHOR did not change significantly, and the accumulation of D-2-HG in vitro was not affected (Fig. 4k), implying that KgtP has no obvious role in D-2-HG export.

Dicarboxylic acid transporters, including YnfM, DcuC, and SucE, were reported to participate in the export of dicarboxylic acids such as glutarate and succinate[38–40]. To determine whether these transporters play roles in D-2-HG export, we knocked out their homologs in *E. coli* W3110(DE3)(Δ*ydiJ*) and detected intracellular and extracellular D-2-HG using DHOR. Knockout of *ynfM* and *dcuC* resulted in 46% and 21% decrease in extracellular D-2-HG concentration, and 19% and 7% increase in fluorescence ratios of DHOR expressed intracellularly, respectively (Fig. 4l). In contrast, the knockout of *yidE* had no such effect (Fig. 4l), indicating the D-2-HG export function of YnfM and DcuC in *E. coli*. Taken together, we showed the ability of DHOR to detect D-2-HG variations in living bacteria and characterized the metabolism and transport of D-2-HG in *E. coli*.

Production of D-2-HG by modulating its metabolism and transport in *E. coli*

D-2-HG can be used as a functionalized building block for polyester after cyclization to an allyl-containing lactide[40,41]. We sought to construct a D-2-HG producer based on the above cognition of D-2-HG metabolism and transport in *E. coli*. The *ydiJ* gene in *E. coli* BL21(DE3) (Δ*lacZ*Δ*frdA*Δ*ldhA*Δ*poxB*Δ*pflB*Δ*pta-ack*), a chassis strain with blocked organic acid production pathway, was replaced with the NAD^+-dependent D-2-HG dehydrogenase encoding gene *hgdH*[42] to simultaneously abolish D-2-HG degradation and achieve D-2-HG overproduction (Fig. 4m). The resulting *E. coli* 7KH produced 15.90 g L^{-1} of D-2-HG from 40 g L^{-1} of glucose after 84 h (Fig. 4n).

Since YnfM is more functional than DcuC for D-2-HG export in *E. coli*, its coding gene was knocked in at the position of the *ycgH* pseudogene and under the control of the T7 promoter. The D-2-HG production of the obtained strain *E. coli* 7KHM increased to 17.20 g L^{-1} (Fig. 4m, o). We also knocked out the D-2-HG importer *kgtP*, and D-2-HG production of the final strain, *E. coli* 8KHM, increased to 18.05 g L^{-1}, with a yield of 0.58 mol mol^{-1} glucose (Fig. 4m, p, q). Thus, the block of D-2-HG import and enhancement of D-2-HG export were both beneficial for D-2-HG production by recombinant *E. coli*. The D-2-HG concentration and yield generated by *E. coli* 8KHM were much higher than those generated by other recombinant strains reported for D-2-HG production[43].

Spatiotemporal resolution of D-2-HG in HEK293FT cells

Basal intracellular concentration of D-2-HG is approximately 25–120 μM in diverse human cell types[44]. IDH mutation can cause at least 20-fold (Fig. 3l) or even 100-fold increase[45] in D-2-HG levels in tumor cells. DHOR exhibited a dynamic detection range of ~ 2 μM–15 mM and was theoretically suitable for the detection of intracellular D-2-HG. We expressed DHOR in human embryonic kidney cells (HEK293FT) to test its applicability for monitoring D-2-HG changes in eukaryotic cells. The fluorescence ratio of DHOR in HEK293FT cells gradually increased and then stabilized within 6 min of D-2-HG addition (Fig. 5a, b). In addition, only exogenous D-2-HG increased the fluorescence ratio of DHOR in a concentration-dependent manner (Fig. 5c–e and Supplementary Fig. 14).

We further assessed the performance of DHOR for detecting endogenous D-2-HG generation by expressing DHOR in HEK293FT cells with wild-type or R132H-mutant IDH1. The fluorescence ratio of DHOR expressed in HEK293FT($IDH1^{R132H}$) cells was obviously higher than that in HEK293FT cells with wild-type IDH1 (Fig. 5f). Measurement of D-2-HG in cell lysates and culture supernatants in parallel experiments using DHOR confirmed that HEK293FT($IDH1^{R132H}$) cells significantly accumulate D-2-HG both in vivo and in vitro (Fig. 5g and Supplementary Fig. 15). Treatment with $IDH1^{R132H}$ inhibitors AGI-5198[46] and GSK864[47] decreased intracellular D-2-HG levels, while $IDH2^{R140Q}$ inhibitor AGI-6780[48] had no inhibitory effect on D-2-HG production by HEK293FT($IDH1^{R132H}$) cells (Fig. 5h, i). Similarly, the D-2-HG accumulation in cell lysates and culture supernatants of HEK293FT($IDH1^{R132H}$) cells was also specifically inhibited by AGI-5198 and GSK864, but not by AGI-6780 (Fig. 5g and Supplementary Fig. 15).

In addition, we developed subcellularly localized DHOR to realize D-2-HG detection in different cellular compartments (Fig. 5j). DHOR targeting cytosol, mitochondria, and nucleus in HEK293FT cells showed increased fluorescence responses primarily in the target subcellular regions to exogenous D-2-HG addition, whereas cpsfYFP exhibited no significant response upon D-2-HG addition (Fig. 5k and Supplementary Figs. 16, 17). We analyzed the subcellular distribution of D-2-HG in HEK293FT cells using DHOR and observed a relatively higher abundance of D-2-HG in the mitochondria than in the cytosol and nucleus (Fig. 5l). The observation is consistent with previous conjecture that mitochondria may be the primary site of D-2-HG accumulation and metabolism in humans because of the localization of D2HGDH[1]. Expressing $IDH1^{R132H}$ or $IDH2^{R172K}$ resulted in obvious increase of D-2-HG in different cellular compartments. Due to the cytoplasmic location of IDH1 and mitochondrial location of IDH2, overexpression of $IDH1^{R132H}$ resulted in higher D-2-HG accumulation in the cytosol and nucleus while overexpression of $IDH2^{R172K}$ caused higher D-2-HG accumulation in the mitochondria (Fig. 5l). Collectively, these results indicate that DHOR is capable of reporting intracellular D-2-HG levels in human cells with spatiotemporal resolution.

Identifying the roles of human SLC22 family transporters in D-2-HG transport

D-2-HG produced by mutant IDHs competitively inhibits 2-KG-dependent dioxygenases (e.g., histone demethylases, DNA dioxygenases, etc.), altering the epigenetic landscape of cells that results in oncogenic transformation[2]. In addition, tumor cells with IDH mutations export intracellularly accumulated D-2-HG into the microenvironment and confer growth advantages to tumor cells through suppressing anti-tumor activity of immune cells[8,9,49,50] (Fig. 6a). For example, tumor-derived D-2-HG inhibits glycolytic enzyme lactate dehydrogenase in $CD8^+$ T cells, altering their glycolysis and impairing cytokine production and cytotoxicity[9]. Probing the transporters involved in the export and import of D-2-HG would be conducive to a better understanding of the interaction between IDH-mutant tumors and the tumor immune microenvironment.

https://doi.org/10.1038/s41467-025-62225-8

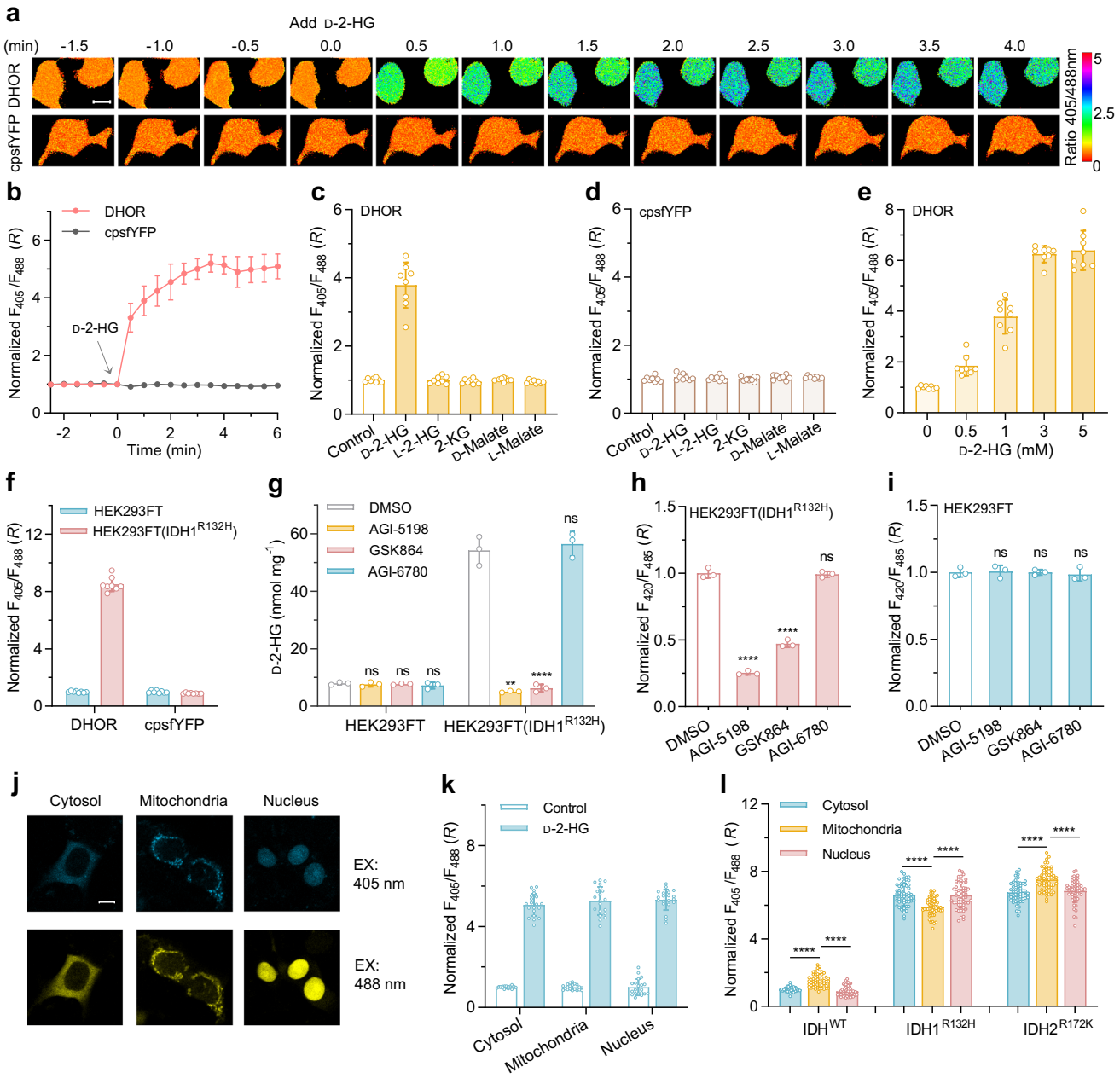

Fig. 5 | Spatiotemporally-resolved detection of D-2-HG in HEK293FT cells. **a**, **b** Sequential ratiometric images (**a**) and fluorescence ratios (**b**) of HEK293FT cells expressing DHOR in response to 3 mM D-2-HG. Scale bar, 10 μm. Data were normalized to the value at time 0 ($n = 4$ cells). **c**, **d** Specificity analysis of DHOR (**c**) or cpsfYFP (**d**) expressed in HEK293FT cells. Indicated compounds (1 mM) were added to cells permeabilized with 80 μM digitonin. Data were normalized to the control group, in which an equal volume of ddH_2O was added to the system instead of any compound ($n = 8$ cells). **e** Fluorescence responses of DHOR expressed in HEK293FT cells to different concentrations of D-2-HG. Cells were permeabilized with 80 μM digitonin. Data were normalized to the value of 0 mM D-2-HG ($n = 8$ cells). **f** Detection of intracellular D-2-HG accumulation caused by $IDH1^{R132H}$ mutation in HEK293FT cells using DHOR. Data were normalized to the values of HEK293FT cells ($n = 8$ cells). **g** Quantification of D-2-HG in cell lysates using DHOR. HEK293FT cells with wild-type or R132H-mutant IDH1 were treated with 0.5 μM inhibitors or an equivalent volume of DMSO for 48 h ($n = 3$ biological replicates). Two-tailed Student's *t* tests, HEK293FT($IDH1^{R132H}$): $P = 3.5 \times 10^{-3}$ for DMSO vs. AGI-5198, $P = 9.4 \times 10^{-5}$ for DMSO vs. GSK864. **h**, **i** Analysis of the effects of inhibitors on intracellular D-2-HG levels in HEK293FT cells with R132H-mutant IDH1 (**h**) or wild-type IDH1 (**i**). Fluorescence ratios were measured using the microplate reader after 24 h of 0.5 μM inhibitor treatment. Data were normalized to the value of the DMSO group ($n = 3$ biological replicates). $P = 5.4 \times 10^{-6}$ for DMSO vs. AGI-5198, $P = 3.8 \times 10^{-5}$ for DMSO vs. GSK864 (**h**). **j** Fluorescence images of subcellularly localized DHOR expressed in HEK293FT cells. Scale bar, 10 μm. **k** Fluorescence responses of subcellularly localized DHOR expressed in HEK293FT cells to 3 mM D-2-HG addition. Cells were permeabilized with 80 μM digitonin. Data were normalized to the value of the control group ($n = 20$ cells). **l** Subcellular distribution of D-2-HG in HEK293FT and HEK293FT expressing $IDH1^{R132H}$ or $IDH2^{R172K}$. Data were corrected by cpsfYFP and normalized to the value of HEK293FT cytosol group ($n = 50$ cells for IDH^{wt}, $n = 54$ cells for $IDH1^{R132H}$ and $IDH2^{R172K}$). IDH^{WT}: $P = 6.7 \times 10^{-13}$ for cytosol vs. mitochondria, $P = 4.9 \times 10^{-15}$ for mitochondria vs nucleus; $IDH1^{R132H}$: $P = 9 \times 10^{-9}$ for cytosol vs. mitochondria, $P = 3.4 \times 10^{-7}$ for mitochondria vs nucleus; $IDH2^{R172K}$: $P = 8.5 \times 10^{-9}$ for cytosol vs. mitochondria, $P = 7.4 \times 10^{-7}$ for mitochondria vs nucleus. All data shown are means ± SD (**b**–**i**, **k**, **l**). ns, no significant difference ($P \geq 0.05$); $^{**}P < 0.01$; $^{****}P < 0.0001$. Source data are provided as a Source Data file.

https://doi.org/10.1038/s41467-025-62225-8

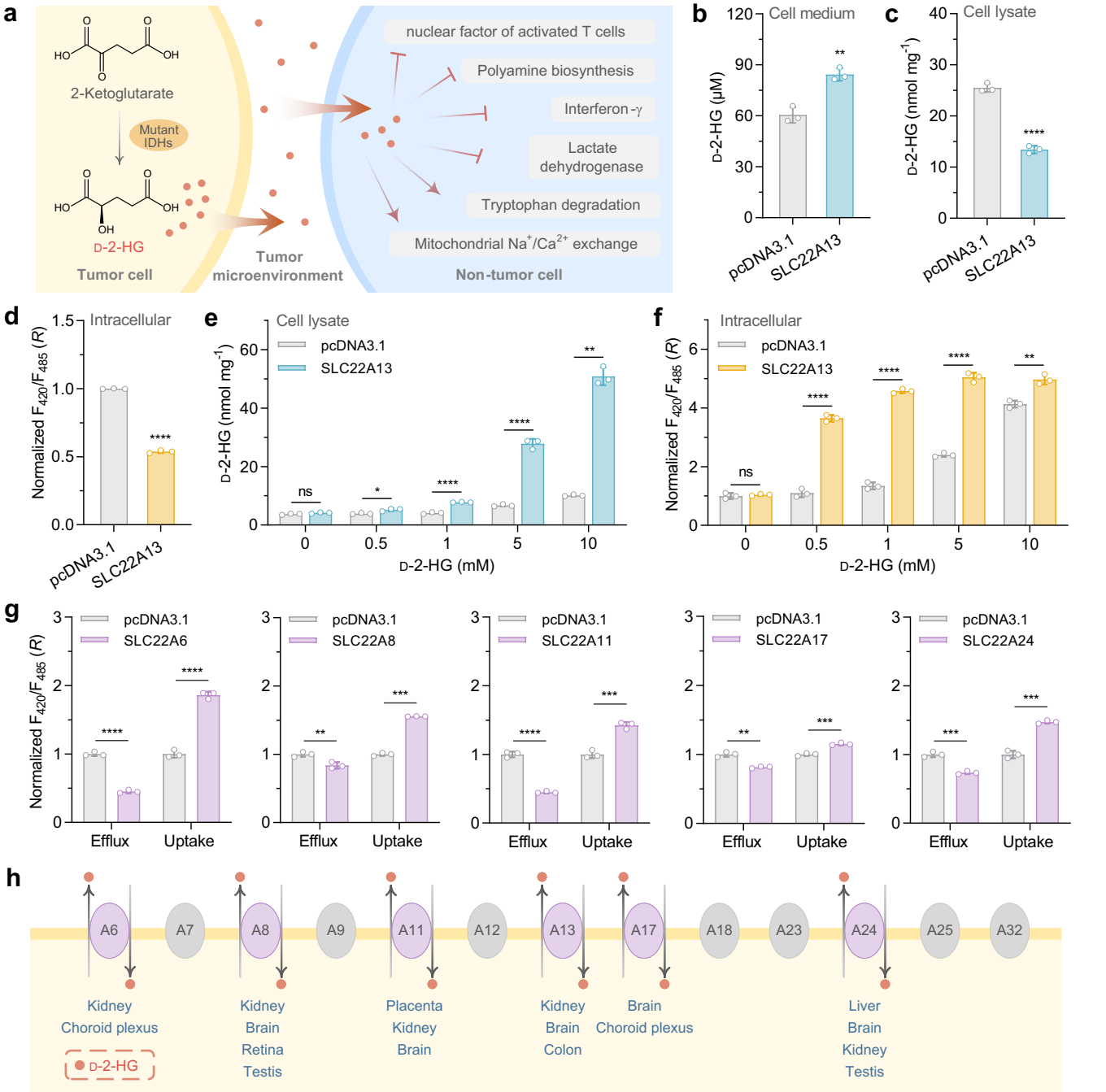

Fig. 6 | Identifying the roles of human SLC22 family transporters in D-2-HG transport. a Schematic diagram of IDH-mutant tumor cells releasing D-2-HG into the microenvironment and affecting non-tumor cells. **b**–**d** D-2-HG efflux function analysis of SLC22A13. Quantification of D-2-HG by DHOR in the culture medium (**b**) and lysates (**c**) of HEK293FT(IDH1^{R132H}) cells expressing pcDNA3.1 empty vector or SLC22A13. Fluorescence ratios of DHOR co-expressed with pcDNA3.1 empty vector or SLC22A13 in HEK293FT(IDH1^{R132H}) cells (**d**). Data were normalized to the value of the pcDNA3.1 group (**d**). Two-tailed Student's *t* tests, $P = 2.3 \times 10^{-3}$ (**b**), $P = 4.9 \times 10^{-5}$ (**c**), $P = 1.6 \times 10^{-7}$ (**d**). **e**, **f** D-2-HG uptake function analysis of SLC22A13. D-2-HG levels in lysates of HEK293FT cells expressing pcDNA3.1 empty vector or SLC22A13 treated with increasing concentrations of D-2-HG (**e**). Fluorescence ratios of DHOR co-expressed with pcDNA3.1 empty vector or SLC22A13 in HEK293FT cells treated with increasing concentrations of D-2-HG (**f**). Data were normalized to the value of the pcDNA3.1 group treated with 0 mM D-2-HG (**f**). 0.5: $P = 1.2 \times 10^{-2}$, 1: $P = 4 \times 10^{-5}$, 5: $P = 2.7 \times 10^{-5}$, 10: $P = 1.7 \times 10^{-3}$ (**e**). 0.5: $P = 1.7 \times 10^{-5}$, 1: $P = 2.2 \times 10^{-6}$, 5: $P = 1.1 \times 10^{-5}$, 10: $P = 2.1 \times 10^{-3}$ (**f**). **g** D-2-HG transport function analysis of SLC22A6, SLC22A8, SLC22A11, SLC22A17, and SLC22A24. Fluorescence ratios of DHOR co-expressed with pcDNA3.1 empty vector or SLC22 family members in HEK293FT(IDH1^{R132H}) cells (for efflux) or in HEK293FT cells treated with 5 mM D-2-HG (for uptake) were measured. Data were normalized to the values of the pcDNA3.1 group. SLC22A6: $P = 1.6 \times 10^{-5}$ for efflux, $P = 3.5 \times 10^{-5}$ for uptake; SLC22A8: $P = 9.3 \times 10^{-3}$ for efflux, $P = 5.2 \times 10^{-4}$ for uptake; SLC22A11: $P = 3.1 \times 10^{-5}$ for efflux, $P = 5.6 \times 10^{-4}$ for uptake; SLC22A17: $P = 1.2 \times 10^{-3}$ for efflux, $P = 7.8 \times 10^{-4}$ for uptake; SLC22A24: $P = 5.7 \times 10^{-4}$ for efflux, $P = 1.6 \times 10^{-4}$ for uptake. **h** Schematic diagram summarizing the D-2-HG transport function of plasma membrane-localized organic anion transporters of the human SLC22 family. Tissue distribution of members with D-2-HG transport function are listed below. All data shown are means ± SD ($n = 3$ biological replicates) (**b**–**g**). ns, no significant difference ($P \geq 0.05$); *$P < 0.05$; **$P < 0.01$; ***$P < 0.001$; ****$P < 0.0001$. Source data are provided as a Source Data file.

Position-specific iterated BLAST analysis indicated that a human plasma membrane-localized OAT, SLC22A13, shares an identity of 28.30% with YnfM from *E. coli*. Therefore, we investigated the function of SLC22A13 in D-2-HG efflux. SLC22A13 overexpression in HEK293FT(IDH1^{R132H}) cells resulted in a 39% increase and a 47% decrease in D-2-HG levels in the culture medium and cell lysates, respectively (Fig. 6b, c). Decreased intracellular D-2-HG level was also directly observed based on DHOR-supported live-cell detection (Fig. 6d). We also analyzed the role of SLC22A13 in D-2-HG uptake by exogenously adding increasing concentrations of D-2-HG to the culture medium of HEK293FT cells overexpressing SLC22A13. Overexpression of SLC22A13 significantly elevated the intracellular D-2-HG concentrations, suggesting that it may be responsible for the bidirectional transport of D-2-HG (Fig. 6e, f).

The SLC22 family can be categorized into OATs, organic cation transporters, and organic zwitterion/cation transporters[51–53]. Besides SLC22A13[54], there are 13 plasma membrane-localized OATs in the human SLC22 family. Thus, we conducted a global analysis of the role of the other 12 plasma membrane-localized OATs in D-2-HG transport. DHOR was co-expressed with OATs in HEK293FT(IDH1^{R132H}) cells to analyze D-2-HG efflux and in HEK293FT cells exposed to 5 mM D-2-HG to analyze D-2-HG influx. Five OATs, SLC22A6, SLC22A8, SLC22A11, SLC22A17, and SLC22A24, were also found to be involved in bidirectional D-2-HG transport across cell membranes, whereas SLC22A7, SLC22A9, SLC22A12, SLC22A18, SLC22A23, SLC22A25, and SLC22A32 were not responsible for D-2-HG import or export (Fig. 6g and Supplementary Fig. 18). Consistent results were obtained by D-2-HG quantification in cell lysate samples using DHOR (Supplementary Figs. 18, 19). OATs with D-2-HG transport function are expressed in various organs, such as the kidney, brain, and liver[52,55] (Fig. 6h), and may participate in D-2-HG-mediated crosstalk between IDH-mutant tumor cells and the microenvironment.

Discussion

D-2-HG is a reliable indicator of cancers with IDH mutations and D2HGA[3–6]. Point-of-care D-2-HG testing is beneficial for assessing the progression and treatment response of these diseases. Miniature MS, enzymatic assays, and Alpha technology have also been applied in in vitro D-2-HG detection. Although miniature MS can achieve rapid intraoperative measurement[34], it requires costly equipment investment and cannot distinguish D-2-HG from L-2-HG. Enzymatic assay of D-2-HG with D2HGDH and resazurin is susceptible to interference from redox-active substances in pending test samples[35,56], while Alpha technology relies on expensive reagent kit and complicated assay system preparation[16]. Recently, convenient and low-cost in vitro L-2-HG assay has been accomplished by cpYFP-based biosensor sfLHGFR[22]. In this study, we developed a cpYFP-based biosensor DHOR, which was able to rapidly quantify D-2-HG in serum and urine with high consistency with LC-MS/MS (Fig. 3d–h). Surgical resection remains the mainstay of treatment for patients with gliomas[57]. Intraoperative D-2-HG detection should allow surgeons to achieve better patient outcomes by directly influencing the extent of surgical resection of IDH-mutant gliomas[34]. Here, we built a compact and inexpensive prototype device for point-of-care D-2-HG testing with DHOR. We demonstrated that the prototype device allowed rapid, accurate, and low-cost D-2-HG detection in glioma samples (Fig. 3i–m). The preliminary proof-of-principle device consists of several detachable components and thus has potential for further miniaturization through integrated design. Large-scale testing is still required for further evaluation of the applicability of the system in clinical diagnosis of D-2-HG-related diseases and guiding decision-making during surgery.

D-2-HG metabolism is involved in various physiological and pathological processes. The basal concentration of intracellular D-2-HG is approximately 25–120 μM in various human cell lines[44], whereas IDH mutations could result in up to 100-fold increases in intracellular D-2-HG levels[45]. Genetically encoded biosensors, DHGFR1.0 and D2HGlo, based on FRET and transcriptional regulator DhdR, have been developed for extracellular and intracellular D-2-HG detection[58,59]. However, both biosensors displayed low response amplitudes and narrow dynamic detection ranges. DHOR exhibited a >1700% fluorescence response, a K_d value ~ 940 μM, and a dynamic detection range of ~ 2 μM–15 mM. Thus, the previously challenging detection of D-2-HG dynamics in living bacteria and human cells can now be achieved using DHOR (Figs. 4a and 5b). Based on the application of DHOR in living human cells, we characterized the inhibitory effects of specific IDH inhibitors on D-2-HG production (Fig. 5h, i), indicating the potential of DHOR in high-throughput screening of new small-molecule drugs targeting IDH mutations.

D-2-HG can also be used as a monomer for biopolymer synthesis[40,41]. The highest reported D-2-HG production of 11.86 g L^{-1} was acquired using metabolic-engineered *Corynebacterium glutamicum*, with a yield of 0.39 mol mol^{-1} glucose[43]. In this study, we identified the D-2-HG catabolic function of YdiJ and the D-2-HG anabolic function of SerA in *E. coli* (Fig. 4d–h). A D-2-HG producer *E. coli* 7KHM was constructed by blocking D-2-HG catabolism and introducing the D-2-HG synthesis enzyme in *E. coli*. We also found that KgtP mediates the uptake of D-2-HG while YnfM and DcuC participate in the efflux of D-2-HG (Fig. 4i–l). Further modulating of D-2-HG transport in *E. coli* 7KHM obviously improved D-2-HG production. The D-2-HG titer of the final strain *E. coli* 8KHM reached 18.05 g L^{-1}, with a yield of 0.58 mol mol^{-1} glucose (Fig. 4p, q). D-2-HG generation is an inevitable step in the biosynthesis of many valuable chemicals like glutarate, pyridoxal 5′-phosphate, and L-serine[10]. Decreasing the intracellular accumulation of D-2-HG through modulation of its transport may also be beneficial for the biosynthesis of chemicals involving D-2-HG generation.

SLC22A13 is highly expressed in the kidney and mediates the uptake of nicotinate, urate, *p*-aminohippurate, etc[54]. Here, we found that SLC22A13 is a homolog of D-2-HG exporter YnfM, and participates in both the export and import of D-2-HG in human cells (Fig. 6b–f). Five other members of the plasma membrane-localized OATs of the human SLC22 family[51,52], SLC22A6, SLC22A8, SLC22A11, SLC22A17, and SLC22A24, were also confirmed to mediate the bidirectional transport of D-2-HG (Fig. 6g, h). These D-2-HG transporters are heterogeneously expressed among different cancer cell lines. For example, SLC22A6 and SLC22A17 are expressed in gliomas; SLC22A6 and SLC22A11 are expressed in leukemia; SLC22A11, SLC22A13, and SLC22A17 are expressed in colon cancer[8,50,60]. D-2-HG exported by IDH-mutant tumor cells can be taken up by T cells and suppressing their anti-tumor activity[8,9]. SLC22A6 is also expressed in human T cells[8]. This D-2-HG transporter may be a potential target and “shut down” to enhance the adaptation of T cells to the high-D-2-HG microenvironment and improve their anti-tumor cytotoxicity. The role of these OATs in the interaction between tumor cells and the microenvironment requires further investigation.

The chimeric antigen receptor-T (CAR-T) cell therapy is considered one of the most promising approaches for anticancer therapy[61]. As mentioned above, CAR-T-based immunotherapy for tumors with IDH mutation may be limited due to the inhibition of oncometabolite D-2-HG toward T cells[62]. The CAR-T cell overexpressing D2HGDH with only the GlcD domain was recently constructed. It exhibited enhanced anti-tumor effectiveness and improved the overall survival of mice bearing IDH-mutant tumors[62]. Besides the GlcD domain, both PP4493 and YdiJ contain an additional GlpC domain. Like the situation in NAD-independent D-lactate dehydrogenase PP4737[63], the GlpC domain in PP4493 and YdiJ may function as an electron transfer component and facilitate the direct utilization of quinone as the electron acceptor. Compared to D2HGDHs with only the GlcD domain, which require electron transfer flavoproteins and ETF-ubiquinone oxidoreductase to accomplish D-2-HG oxidation[11], PP4493 and YdiJ may be more suitable for engineered CAR-T cells to eliminate D-2-HG. In addition, we also identified the D-2-HG regulator

HgcR and several D-2-HG transporters in this study. These elements can be integrated with the D-2-HG catabolic enzymes PP4493 and YdiJ to construct a synthetic circuit for sensing, transporting, and catabolizing D-2-HG. The synthetic circuit may be introduced into CAR-T cells to simultaneously eliminate oncometabolite D-2-HG and provide 2-KG for the engineered cells.

In summary, we developed a genetically encoded D-2-HG biosensor DHOR with high responsiveness, brightness, and specificity, which was able to rapidly quantify D-2-HG in vitro and detect D-2-HG in living cells with spatial and temporal resolution. Based on DHOR, we built a proof-of-principle device that enables the accurate, fast, and cost-effective assay of D-2-HG in serum, urine, and glioma tissue samples, providing a prototype for point-of-care testing. Moreover, we identified potential D-2-HG transporters in *E. coli* and human cells, and improved fermentative D-2-HG production by *E. coli* through modulating its transport. We also demonstrated that DHOR can detect the inhibitory effect of developed inhibitors on mutant IDH and may be used in rapid high-throughput screening of potential medicines targeting diseases with IDH mutation. We anticipate that DHOR may serve as a versatile tool for investigating the metabolism, function, and carcinogenesis of D-2-HG, as well as for the diagnosis, prognosis, and treatment of D-2-HG-related diseases.

Methods

Ethical statement

All procedures were performed in compliance with relevant laws and institutional guidelines. Animal studies were approved by the Second Hospital of Shandong University Ethics Committees (Approval No. KYLL-2022A128). Human subjects were approved by the Medical Ethics Committee of the First Hospital of China Medical University (Approval No. [2022]-No.6) and the Second Hospital of Shandong University Ethics Committees (Approval No. KYLL-2023LW019). Written informed consent was obtained for experimentation with human subjects. For studies involving animals and human research participants, gender and/or sex was not considered in the study design.

Bacteria and culture conditions

Bacterial strains used in this study are listed in Supplementary Data 1. *P. putida* KT2440 and its derivatives were cultured in Luria-Bertani (LB) broth or minimal salt medium (MSM)[64] with indicated carbon sources at 30 °C and 200 rpm. *E. coli* and its derivatives were cultured in LB broth or MSM with indicated carbon sources at 37 °C and 180 rpm. Antibiotics were used at the following concentrations: kanamycin, 50 μg mL^{-1}; carbenicillin, 100 μg mL^{-1}; Ampicillin, 100 μg mL^{-1}; chloramphenicol, 40 μg mL^{-1}; Spectinomycin, 50 μg mL^{-1}.

Reagents

D-2-Hydroxyglutaric acid disodium salt (D-2-HG, CAS 103404-90-6) and L-2-hydroxyglutaric acid disodium salt (L-2-HG, CAS 63512-50-5) used as carbon sources were purchased from Shanghai Hanhong Scientific Co., Ltd. and Chengdu Huaxia Chemical Reagent Co., Ltd., respectively. D-2-HG (16859), L-2-HG (90790), 2-ketoglutarate (75890), glutarate (G3407), glutaconate (369535), L-lysine (Ll5501), D-malate (02300), L-malate (112577), D-lactate (71716), L-lactate (L7022), pyruvate (P5280), oxaloacetate (O7753), citrate (C3674), isocitrate (I1252), succinate (398055), fumarate (47910), cis-aconitate (A3412) used in this study were purchased from Sigma-Aldrich (USA). D-Lysine (D4110) was purchased from Beijing Solarbio Science & Technology Co., Ltd. D-2-Hydroxybutyrate (R919859) and L-2-hydroxybutyrate (S839641) were purchased from Macklin (China). All other chemicals were of analytical reagent grade.

Cell lines and gene expression

The HEK293FT (CL-0313) and U87MG (CL-0238) cell lines were purchased from Procell Life Science & Technology Co., Ltd (China). HEK293FT and U87MG cell lines stably expressing $IDH1^{R132H}$ were constructed in our previous study[16,35]. HEK293FT cells were cultured in high-glucose Dulbecco's Modified Eagle Medium (DMEM) (Gibco, USA) supplemented with 10% (v/v) fetal bovine serum (Biological Industries, Israel) and 1% (v/v) penicillin-streptomycin (Gibco, USA). U87MG cells were cultured in complete medium (PM150410, Procell, China) supplemented with 10% (v/v) fetal bovine serum and 1% (v/v) penicillin-streptomycin. All cells were cultured at 37 °C in 5% CO_2 humidified atmosphere.

HEK293FT cells were cultured to 70–90% confluency with antibiotic-free medium before plasmid transfection. The Lipofectamine 3000 transfection kit (ThermoFisher, USA) was used for gene transient expression according to the manufacturer's instructions, with a Lipofectamine 3000:P3000:DNA ratio of 1.5:1.5:1 (μL:μL:μg). At 6 h post-transfection, the medium was replaced with fresh culture medium.

Animal studies

Mice were housed in a standard environment, which was characterized by a 12 h light/dark cycle, 22–26 °C, and 40–60% humidity with food and water available ad libitum. Five-week-old male Balb/c nude mice (Charles River, USA) were implanted subcutaneously in the flanks with 2×10^6 U87MG cells with wild-type or R132H-mutant IDH1. After 26 days, tumors reached about 100–200 mm^3 and mice were sacrificed on day 31. The maximal tumor size of 1500 mm^3 was permitted by the Second Hospital of Shandong University Ethics Committees. We confirm that the maximal tumor size was not exceeded in any of the experiments.

Construction of *P. putida* KT2440 and *E. coli* mutants

The plasmids and primers used in this study are listed in Supplementary Data 1, respectively. *P. putida* KT2440 mutants were constructed using pK18*mobsacB*[65]-mediated allelic exchange. A truncated fragment of the target gene was cloned into pK18*mobsacB*. The resulting plasmid was transferred into *P. putida* KT2440 through electroporation. The single-crossover mutants were selected on LB plates with kanamycin. The double-crossover mutants were selected on LB plates with 10% (w/v) sucrose.

E. coli W3110(DE3) mutants were constructed using Red system-mediated recombination[66]. The recombinant fragment consisting of the upstream homologous arm, kanamycin resistance cassette (cloned from pKD4 plasmid), and the downstream homologous arm was transferred into *E. coli* W3110(DE3) expressing the pTKRed plasmid by electroporation. The kanamycin resistance cassette integrated into the genome was excised by pCP20-mediated recombination. The pCP20 plasmid is temperature-sensitive and can be cured through growth at 42 °C.

E. coli BL21(DE3) mutants were constructed using the pEcCas-pEcgRNA system-mediated recombination[67]. The sgRNA was designed using the online website (http://chopchop.cbu.uib.no/) and expressed by the pEcgRNA plasmid. The knockout fragment was generated by PCR recombination of the upstream and downstream arms of the target gene. For gene knockin, the target gene was first cloned into the multiple cloning sites-2 of the pETDuet-1 plasmid with a deleted lac operator, and then the knockin fragment consisting of the upstream arm, T7 promoter-2, target gene, T7 terminator, and the downstream arm was obtained by PCR. Then, 1000 ng knockout/knockin fragment and 250 ng pEcgRNA plasmid were transferred into *E. coli* BL21(DE3) derivatives expressing the pEcCas plasmid by electroporation. The pEcgRNA and pEcCas plasmid can be cured by successive cultivation in LB liquid with 10 mM rhamnose and LB plate with 10 g L^{-1} sucrose.

Quantification of 2-HG, pyruvate, and acetate using HPLC

The high-performance liquid chromatography (HPLC) system (LC-20AT, Shimadzu, Japan) was equipped with an Aminex HPX-87H column (300 × 7.8 mm, Bio-Rad, USA) and a refractive index detector. Samples were boiled at 105 °C for 10 min and centrifuged at 18,000 × *g*

for 15 min. The supernatants were filtered and analyzed with 10 mM H_2SO_4 as the mobile phase at a flow rate of 0.4 mL min^{-1}.

Quantification of lysine using HPLC

The HPLC system (1100, Agilent, USA) was equipped with a ZORBAX SB-C18 column (5 µm, 4.6 × 150 mm, Agilent, USA). Samples were boiled at 105 °C for 10 min and centrifuged at 18,000 × *g* for 15 min. Then, 400 µL of supernatant was mixed with 200 µL of ethylamine-acetonitrile solution (1 M) and 200 µL of phenylisothiocyanate-acetonitrile solution (100 mM). After incubation at room temperature for 1 h, 800 µL of n-hexane was added. The mixture was vortexed and centrifuged at 15,000 × *g* for 2 min. The lower phase solution was filtered and analyzed with 100 mM ammonium acetate-acetonitrile (97:3, v/v, pH 6.5) as mobile phase A and 80% (v/v) acetonitrile as mobile phase B at a flow rate of 0.6 mL min^{-1}. Gradient elution was performed from 18% to 30% B from 0 to 20 min and maintained at 30% B from 20 to 40 min.

Expression analysis of *d2hgdh*

The gene of pGFPmut2 was cloned from plasmid pMRP9-1[21] and fused with a flexible linker (GSAGSAAGSGEF)[68] at the N-terminus. The recombination fragment was inserted into the genome of *P. putida* KT2440 before stop codons of *pp5154* and *pp4493* through pK18*mobsacB*-mediated allelic exchange. Corresponding strains were grown to the stationary phase in MSM with the indicated carbon sources. Bacterial culture was collected and resuspended with an equal volume of saline (8.5 g L^{-1} NaCl). Then, 100 µL of suspension was transferred to a black 96-well plate (PerkinElmer, USA) and the 509 nm emission was measured at 488 nm excitation using the Ensight microplate reader (PerkinElmer, USA). The fluorescence intensities were normalized to the optical density at 600 nm (OD_{600}).

Protein expression and purification

The purification of HgcR was taken as an example. *E. coli* BL21(DE3) harboring pET28a-HgcR was grown to OD_{600} of 0.6–0.8 in LB broth at 37 °C, 180 rpm. Then, 0.9 mM isopropyl-β-D-1-thiogalactopyranoside (IPTG) was added to induce protein expression at 23 °C, 160 rpm for 14 h. Bacterial cultures were harvested, washed once with phosphate-buffered saline (PBS), and resuspended in buffer A (20 mM sodium phosphate, 500 mM NaCl, and 20 mM imidazole, pH 7.4) containing 10% (v/v) glycerol and 1 mM phenylmethylsulfonyl fluoride (PMSF). Bacterial suspension was lysed using the AH-BASIC high-pressure homogenizer (ATS, China) at 4 °C. The lysate was centrifuged at 12,000 × *g* for 40 min at 4 °C. The supernatants were loaded onto a 5 mL HisTrap HP column (GE Healthcare, USA) equilibrated with buffer A, and eluted with buffer B (20 mM sodium phosphate, 500 mM NaCl, and 500 mM imidazole, pH 7.4). The purified protein was analyzed by 13% SDS-PAGE. Glycerol was added to a final concentration of 10% (v/v), and protein aliquots were snap frozen and stored at − 80 °C. The protein concentration was determined using the Bradford protein assay kit (Sangon, China).

Gel filtration chromatography

Gel filtration chromatography was performed using a Superdex 200 10/300 GL column (GE Healthcare, USA). The column was equilibrated with 50 mM sodium phosphate buffer (pH 7.2) containing 150 mM NaCl, with or without the addition of 3 mM D-2-HG. The standards used were ferritin (440 kDa), aldolase (158 kDa), conalbumin (75 kDa), ovalbumin (43 kDa), and aprotinin (6.5 kDa).

Electrophoretic mobility shift assays (EMSAs)

The DNA fragments of the *pp4493* promoter were amplified from the genomic DNA of *P. putida* KT2440 using primers HgcR-EMSA-F/R. For the binding assay, the 20 µL reaction system contained 5 nM DNA fragments and a gradient concentration of purified HgcR in the binding buffer (Tolo Biotech Co., Ltd., China). To analyze substrate specificity of HgcR, the 20 µL reaction system included 5 nM DNA fragments, 300 nM HgcR, and 10 mM indicated compounds. The mixed solutions were incubated at 30 °C for 30 min, and electrophoresis was performed using 6% native polyacrylamide gels with 170 V in 1 × tris-borate EDTA (TBE, pH 8.3) for 40–50 min on ice. The gels were stained with SYBR green I (TaKaRa, Japan) and then imaged using G:BOX F3 gel documentation system (Syngene, USA).

DNase I footprinting

DNase I footprinting experiments were carried out by Shanghai Biotechnology Corporation (China) according to previously described[69]. The promoter fragment of *pp4493* was cloned into the pEASY-Blunt plasmid using the pEASY-Blunt Cloning Kit (TransGen, China) to obtain pEASY-Blunt-HgcR. FAM-labeled promoter fragment was amplified with 2 × TOLO HIFI DNA polymerase premix (TOLO Biotech, Shanghai) from pEASY-Blunt-P_{pp4493} using universal primer pair M13F-FAM/M13R. The 40 µL reaction solution contained 300 ng purified FAM-labeled fragment, 2 µg purified HgcR, and 0 or 20 mM D-2-HG in EMSA binding buffer. The mixtures were incubated at 25 °C for 30 min, digested by adding 10 µL of DNase I solution (0.015 U DNase I [Promega, USA], 100 nmol freshly prepared $CaCl_2$), incubated for another 1 min at 37 °C, then stopped by adding 140 µL of DNase stop solution (0.15% [w/v] SDS, 200 mM sodium acetate, 30 mM EDTA). Samples were extracted with phenol/chloroform, precipitated with ethanol, resuspended in 30 µL of ultra-pure water. For both digested DNA fragments and sequencing products, 1 µL of each sample was added to 8.5 µL of HiDi formamide and 0.5 µL of GeneScan-LIZ500 size standards (Applied Biosystems, USA), and analyzed with 3130XL DNA analyzer and Peak Scanner software v1.0 (Applied Biosystems, USA).

Construction and optimization of DHOR

Insertion sites screening. The upstream arm of *hgcR*, cpYFP fragment, and the downstream arm of *hgcR* were overlapped and cloned into pET-28a(+) plasmid between BamHI and XhoI restriction sites using T5 exonuclease DNA assembly method[70]. The resulting plasmids were transferred into *E. coli* BL21(DE3). Corrected transformants were inoculated into 50 mL LB broth, and protein expression was induced overnight. Then, 40 mL of bacterial cultures were collected by centrifugation and resuspended to an OD_{600} of 16 using PBS containing 1 mM PMSF. Bacterial suspensions were lysed by ultrasonic disruption (JY92-II, Scientz Biotechnology, China) on ice and centrifuged at 12,000 × *g* for 5 min at 4 °C. The supernatant was mixed with 4 mM D-2-HG at a volume ratio of 3:1. Then, 100 µL of the mixture was transferred to a black 96-well plate and incubated at room temperature for 10 min. The 528 nm emissions at 420 nm and 485 nm excitation were detected using the microplate reader. Selected variants were further purified to determine dose-response curves.

DNA binding domain truncation and superfolder sites substitution. The truncated fragment was amplified using pET28a-$DHOR_{0.1}$ as the template and cloned into pET-28a(+) plasmid between BamHI and XhoI restriction sites. To introduce superfolder sites (S30R, Y39N, N105T, and Y145F, the number of the substituted amino acids in cpYFP corresponds to the sequence of the original YFP), the upstream and downstream parts of cpsfYFP were amplified with primer pairs cpsfYFP-up-F/R and cpsfYFP-down-F/R, respectively, and then overlapped. The DNA fragment of the plasmid backbone was amplified by inverse PCR with the primer pair cpsfYFP-inverse PCR-F/R using pET28a-$DHOR_{0.2}$ as the template and ligated to cpsfYFP. The resulting plasmids were transferred into *E. coli* BL21(DE3). Variants were purified to determine dose-response curves.

Random linker screen. The DNA fragment of the plasmid backbone was amplified by inverse PCR with primer pair mlinker-inverse PCR-F/R using pET28a-$DHOR_{0.3}$ as the template. cpsfYFP fragments were

amplified using primers containing randomized NNB codons in N-terminal linker primers and VNN codons in C-terminal linker primers, which were ligated to the plasmid backbone and transferred into *E. coli* BL21(DE3). Transformants were evenly spread on LB plates containing kanamycin and incubated overnight at 37 °C and then 24 h at 23 °C. Bright colonies were picked to 1 mL of LB broth, then inoculated into 15 mL of LB broth and induced by 0.9 mM IPTG at an OD_{600} of 0.6 overnight. Bacterial cultures were collected by centrifuging, resuspended with 2.5 mL PBS containing 1 mM PMSF, and transferred to 48 deep-well plates. Bacterial suspensions were lysed using SCIENTZ-48TD multi-channel ultrasonic disrupter (SCIENTZ, China) on ice. The lysate in each well was collected and centrifuged at 12,000 × *g* for 5 min at 4 °C. The supernatant was mixed with 4 mM D-2-HG at a volume ratio of 3:1. Then, 100 µL of the mixture was transferred to a black 96-well plate and incubated at room temperature for 10 min. Fluorescence was detected using the microplate reader. Selected variants were further purified to determine dose-response curves.

Characterization of DHOR in vitro

Dose-response curve. DHOR was diluted with 100 mM potassium phosphate buffer (18.3032 g L^{-1} $K_2HPO_4{\cdot}3H_2O$, 2.6946 g L^{-1} KH_2PO_4) to a final concentration of 1 µM and mixed with gradient concentrations of D-2-HG at a volume ratio of 3:1. The mixture was transferred to a black 96 (100 µL) or 384 (20 µL) well plate and incubated at room temperature for 10 min. 528 nm emissions at 420 nm and 485 nm excitation were detected using the microplate reader. The fluorescence emission ratio (F_{420nm}/F_{485nm}) of 420 nm and 485 nm excitation was plotted against the D-2-HG concentration and fitted using Origin software (OriginLab, USA) according to the following formula:

$$R = R_{max} + \frac{R_{min} - R_{max}}{1 + ([\text{D-2-HG}]/K_d)^p}$$

R, experimental F_{420nm}/F_{485nm}; R_{max}, the maximum F_{420nm}/F_{485nm}; R_{min}, the minimum F_{420nm}/F_{485nm}; [D-2-HG], the concentration of D-2-HG; K_d, apparent dissociation constant; p, Hill slope. The response magnitudes (maximum ratio changes, ΔR_{max}) were calculated as $\Delta R_{max} = (R_{max} - R_{min})/R_{min}$.

Spectroscopy. Fluorescence spectrum of DHOR was scanned using 1 µM DHOR in the presence or absence of 1 mM D-2-HG. For excitation spectrum analysis, 530 nm emission was excited from 350 nm to 514 nm in steps of 2 nm. For emission spectrum analysis, 505 nm to 599 nm emission was detected in steps of 2 nm at 420 nm and 485 nm excitation, respectively.

Extinction coefficient. The extinction coefficient was measured as previously described[26]. DHOR was diluted in 100 mM potassium phosphate buffer. Absorption spectra were recorded from 300 nm to 650 nm using the Ultrospec 2100 pro UV-VIS spectrophotometer (Amersham Biosciences, USA). The extinction coefficients (ε) were determined using the formula: $\varepsilon = Abs \times c(\text{M})^{-1} \times l(\text{cm})^{-1}$, where Abs is the optical density at the absorption maximum, c is the molar concentration of protein, and l is the optical path length. D-2-HG was added to the assay system at a final concentration of 15 mM as required.

Quantum yield. The quantum yield was measured as previously described[26]. DHOR and EGFP were diluted to various concentrations in 100 mM potassium phosphate buffer. The emission spectra were excited at 420 nm and recorded from 435 nm to 650 nm, or excited at 480 nm and recorded from 495 nm to 650 nm. The absorbance at 420 nm and 480 nm of the corresponding solution was measured using Ultrospec 2100 pro UV-VIS spectrophotometer. The quantum yield of DHOR (QY_{DHOR}) was determined using the formula: $QY_{DHOR} = QY_{EGFP} \times (m_{DHOR}/m_{EGFP})$, where m is the slope obtained by linear fitting of the integrated fluorescence intensity (defined as the area of the fluorescence spectrum) against the absorbance, and QY_{EGFP} is 0.6. D-2-HG was added to the assay system at a final concentration of 15 mM as required.

Specificity. Fluorescence responses of DHOR to 500 µM indicated compounds were detected in the absence or presence of 1 mM D-2-HG. Dose-response curves of DHOR toward D-2-HG were determined in the presence or absence of 500 µM 2-KG or L-2-HG.

Stability. For temperature stability, fluorescence ratios of DHOR to 30 µM and 5 mM D-2-HG were detected after 10 min incubation at indicated temperatures. For pH stability, dose-dependent curves of DHOR toward D-2-HG were determined in potassium phosphate buffer adjusted to different pH. The fluorescence ratio of DHOR was divided by that of cpsfYFP in the parallel experiment for pH correction.

Reversibility. The initial reaction system contained 2 µM DHOR or cpsfYFP and 4 mM pyruvate in potassium phosphate buffer. 200 µM D-2-HG and 0.5 mg mL^{-1} DLD3 were added sequentially. Fluorescence ratios were measured consistently with an interval of 20 s.

Molecular dynamics simulations

The structures of DHOR monomer and dimer were modeled using AlphaFold3[71]. 3D structure of D-2-HG was downloaded from PubChem database (PubChem CID: 439391). The ligand-binding pocket of dimeric DHOR was predicted using DoGSiteScorer web server from ProteinsPlus (https://proteins.plus)[72,73]. Molecular docking and molecular dynamics simulations were performed using Schrödinger 2023-1 software suite (Meastro version 13.5.128, MMshare version 6.1.128). D-2-HG and DHOR dimer were minimized and optimized using LigPrep and Protein Preparation Workflow, respectively. The docking receptor grid was created using Receptor Grid Generation according to predicted ligand binding pockets. Molecular docking was performed using the Glide standard precision mode with default settings. Both D-2-HG-free and D-2-HG-bound systems were built using Desmond System Builder. The TIP3P solvent model was employed, with a cubic water box size of 17 × 17 × 17 Å for the monomer and 25 × 25 × 25 Å for the dimer. Counterions (Na^+, Cl^-) were added to neutralize the system charge and yield an ionic strength of 150 mM. The OPLS4 force field was applied in all steps. Simulations were carried out for 150 ns in the NPT ensemble at 300 K and 1 bar pressure using Desmond Molecular Dynamics. The initial and final configurations for molecular dynamics simulations are available in Supplementary Data 2. CAVER 3.0 PyMol plugin (https://www.caver.cz/) was used for tunnel calculation[74]. PyMOL (PyMOL Molecular Graphics System, Version 3.0 Schrödinger, LLC) and UCSF ChimeraX 1.9[75] were used for structural analysis and for generating figures.

Determination of D-2-HG in serum, urine, and tumor tissues

Sample preparation. Human serum (SL010) was purchased from Beijing Solarbio Science & Technology Co., Ltd. and filtered through a 0.22 µm filter before use. Human urine was collected from a healthy volunteer (approved by the Second Hospital of Shandong University Ethics Committees) and filtered through a 0.22 µm filter before use. Tumor samples from glioma patients were obtained from the First Hospital of China Medical University and approved by its Medical Ethics Committee. IDH wild-type glioma cohort consists of 11 individuals (eight males, three females). IDH-mutant glioma cohort consists of 10 individuals (six males, four females). Tumor tissues (approximately 100 mg) from mice or human were homogenized in 400 µL potassium phosphate buffer using a hand grinder (OSE-Y50, TIANGEN, China), centrifuged at 20,000 × *g* for 1 min, and the resulting supernatants were filtered through a 0.22 µm filter (if the user wants to process a large number of samples or the resulting sample volume is

too small for filtration, the homogenate can be boiled at 105 °C for 5–10 min and then centrifuged at 20,000 × *g* for 3 min to obtain the supernatant for detection).

D-2-HG quantification using the prototype device. The optics and electronics of the device were purchased from Guangzhou Jingyi Optoelectronics Technology Co., Ltd. (China). The integrating sphere (φ 84 mm) was connected to the spectrometer (USB6500) through 1000 μM-core diameter quartz fibers. For D-2-HG detection, 15 μL of samples were directly mixed with 45 μL of DHOR (final concentration of 17 μM, diluted with potassium phosphate buffer) in PCR tubes. The emission spectra of the sample excited by 415 nm and 475 nm LEDs (5 W) were recorded, respectively. The background value (the signal value without sample and light source) was subtracted from 515 nm emission (F_{415}) excited by 415 nm LED and 540 nm emission (F_{475}) excited by 475 nm LED, respectively. The concentration of D-2-HG was calculated by fitting the fluorescence emission ratio (F_{415}/F_{475}) to the dose-dependent curve made by the prototype device.

D-2-HG quantification using LC-MS/MS. For LC-MS/MS analysis, pretreated serum, urine, and tumor samples requires further deproteinization: serum and tumor samples were mixed with an equal volume of methanol, vortexed for 2 min, and centrifuged at 18,000 × *g* for 15 min; urine samples were boiled at 105 °C for 15 min and centrifuged at 18,000 × *g* for 15 min. The resulting supernatants were filtered through a 0.22 μm filter. LC-MS/MS was performed using a high-performance liquid chromatography-triple quadrupole mass spectrometry (SCIEX Triple Quad™ 5500 + System – QTRAP, AB SCIEX, USA) equipped with a Chirobiotic R column (250 mm length × 4.6 mm I.D., 5 mm silica gel particles bonded to the macrocyclic glycopeptide ristocetin A) (Supelco Analytical, USA) in the negative ion mode. Stable isotope labeled D,L-2-hydroxyglutarate disodium salt (2,3,3-D_3-2-HG, Cambridge Isotope Laboratories, Inc., USA) at a final concentration of 10 μM was added to the samples as an internal standard and filtered for LC-MS/MS analysis. The mobile phase consisted of methanol and 0.1% triethylamine adjusted to pH 4.5 with acetate (5:95, v:v). The total analysis time was 30 min with a flow rate of 0.5 mL min^{-1}. Monitored transitions for 2-HG and D_3-2-HG were 147.0 → 129.0 m/z and 150.0 → 132.0 m/z, respectively. The data files generated by LC-MS/MS were processed using SCIEX OS Version 1.7.0.36606 (AB SCIEX, USA).

Application of DHOR in *E. coli*

In vivo *D–2-HG detection*. *E. coli* W3110(DE3) harboring pET28a-DHOR or pET28a-cpsfYFP was grown to OD_{600} of 0.6–0.8 in LB broth at 37 °C, 180 rpm. Then, 0.9 mM IPTG was added to induce protein expression overnight at 23 °C, 160 rpm. Bacterial cultures were harvested, washed once with PBS, suspended in MSM containing indicated carbon sources to an OD_{600} of 5.0, and transferred to a black 96-well plate (150 μL per well). Fluorescence intensities were monitored every 5 min or detected after 10 min incubation using the microplate reader with continuous shaking at 30 °C. Fluorescence ratios of DHOR were corrected by cpsfYFP in parallel experiments.

In vitro *D-2-HG detection*. For D-2-HG quantification of culture medium samples, the dose-response curve was made using D-2-HG serially diluted with the same medium. To avoid significant pH changes induced by acidic by-products excreted during the growth of the strains, the detection of extracellular samples by DHOR (final concentration of 1 μM, diluted with potassium phosphate buffer) was corrected by parallel experiments with cpsfYFP.

D-2-HG batch fermentation

Fermentation was conducted in a 1 L bioreactor (Multifors 2, Infors AG, Switzerland) with 0.8 L of medium. The seed culture was inoculated (10%, v/v) into the fermentation medium containing 40 g L^{-1} glucose and 5 g L^{-1} lactose. The cultivation was carried out at 37 °C with an agitation speed of 400 rpm and an airflow rate of 1.5 vvm. The pH was maintained at 6.8 by automatic addition of 10 M NaOH. Samples were taken every 3 h to measure OD_{600} and concentrations of glucose, D-2-HG, and by-products. The concentration of glucose was assayed using SBA-40D bioanalyzer (Shandong Academy of Sciences, China). D-2-HG and by-products were analyzed by HPLC. The fermentation medium containing 13.5 g L^{-1} KH_2PO_4, 4 g L^{-1} $(NH_4)_2HPO_4$, 1.7 g L^{-1} citrate, 1.4 g L^{-1} $MgSO_4{\cdot}7H_2O$, 4.5 mg L^{-1} vitamin B1, and 10 mL L^{-1} 100 × multi-component metal ion solution (10 g L^{-1} $FeSO_4{\cdot}7H_2O$, 2.2 g L^{-1} $ZnSO_4{\cdot}7H_2O$, 1.0 g L^{-1} $CuSO_4{\cdot}5H_2O$, 0.38 g L^{-1} $MnSO_4{\cdot}H_2O$, 0.02 g L^{-1} $Na_2B_4O_7{\cdot}10H_2O$, 0.1 g L^{-1} $[NH_4]_6Mo_7O_{24}$, 2.0 g L^{-1} $CaCl_2$, pH 2.8).

Preparation of cell lysate samples

Inhibitor treatment. HEK293FT and HEK293FT($IDH1^{R132H}$) cells were seeded into 6-well plates with 2.5 mL DMEM per well and grown to 70–90% confluency. Then, the culture medium was replaced with fresh DMEM containing 0.5 μM AGI-5198 (HY-18082, MedChemExpress, USA), GSK864 (HY-19540, MedChemExpress, USA), AGI-6780 (S7241, Selleck, USA), or equal volumes of DMSO (vehicle, D2650, Sigma-Aldrich, USA).

SLC22 family members overexpression. The protein sequence accession numbers of SLC22 family members used in this study are listed in Supplementary Data 1. All coding sequences preceded by Kozak sequence (GCCACC) were synthesized and cloned into pcDNA3.1(+) plasmid by Jiutian Gene Technology Co., Ltd (Tianjin, China). Plasmids were transfected into HEK293FT and HEK293FT($IDH1^{R132H}$) cells using Lipofectamine 3000. For D-2-HG uptake function assays, indicated concentrations of D-2-HG were added after 6 h transfection.

Sample preparation. After 48 h of cultivation, the medium was collected and centrifuged at 12,000 × *g* for 5 min. The cell culture supernatant was used for detection. Cells were washed with PBS, treated with 250 μL cell lysis buffer (P0013, Beyotime, China) for 5 min, centrifuged at 12,000 × *g* for 10 min at 4 °C to remove cell debris, and the supernatants were detected by DHOR (final concentration of 1 μM, diluted with potassium phosphate buffer). The dose-responsive curve was made using D-2-HG serially diluted with the cell lysis buffer. Protein concentrations of cell lysates were determined by enhanced BCA protein assay kit (P0010, Beyotime, China) and used to normalize D-2-HG quantitative results of cell lysate samples.

Application of DHOR in HEK293FT cells

Confocal imaging. Cells were plated on poly-L-lysine (Sigma-Aldrich, USA) pre-coated 35 mm glass-bottom dishes and grown to 70–90% confluency. pcDNA3.1(+) plasmid expressing codon optimized DHOR or cpsfYFP with Kozak sequence (GCCACC) was transfected into HEK293FT cells using Lipofectamine 3000. After 24–48 h transfection, fluorescence imaging was carried out by excitation with 405 nm and 488 nm lasers using an LSM900 confocal microscope (Zeiss, Germany) with a 20 ×/0.8 objective lens. To analyze the response of DHOR or cpsfYFP to exogenous D-2-HG, cells were washed twice with pre-warmed HHBSS buffer (1 × Hanks' Balanced Salt Solution [14025-092, Gibco] supplemented with 10 mM HEPES [15630-106, Gibco]) prior to treatment by 80 μM digitonin (D141, Sigma-Aldrich, USA) for 6 min. Images were acquired continuously at 30 s intervals or after 5 min of D-2-HG addition. In other cases, cell medium was removed and images were taken directly. ZEN blue software (Zeiss, Germany) was used to analyze the images. ImageJ software[76] was used to process pixel-by-pixel ratio images.

96-well plate assays. Cells were seeded into black 96-well plate (655086, Greiner Bio-One, Germany) and grown to 70–90% confluency

for transfection. After 6 h, the medium was replaced with fresh DMEM containing 0.5 μM inhibitors for another 24 h treatment (for inhibitor analysis), or fresh DMEM with or without D-2-HG for another 48 h treatment (for D-2-HG transport function analysis of SLC22 family members). The medium was removed and cells were incubated with 100 μL HHBSS buffer in the microplate reader for 10 min at 30 °C before detection. Fluorescence ratios of DHOR were corrected by cpsfYFP in parallel experiments.

Subcellular localization of DHOR

The plasmid pcDNA3.1$^{(+)}$ was used for subcellular expression of DHOR or cpsfYFP in HEK293FT cells. For cytoplasmic localization, two repeats of MAPKK nuclear export signal $(MALQKKLEELELDEQQRKRLEDL)_2$ were fused to the N-terminus of DHOR or cpsfYFP. For mitochondrial localization, a COX4 mitochondrial targeting signal (MLATRVFSLVGKRAISTSVCVRAH) was fused to the N-terminus of DHOR or cpsfYFP. For nuclear targeting, three repeats of the SV40 large T antigen nuclear localization signal $(DPKKKRKV)_3$ were fused to the C-terminus of DHOR or cpsfYFP.

Statistical & reproducibility

Data analysis was performed with Graphpad Prism 9.5.1 (Graphpad Software, USA). The statistical significance was analyzed by two-tailed Student's *t* test. A *P*-value less than 0.05 was considered significant ($^*P < 0.05$, $^{**}P < 0.01$; $^{***}P < 0.001$, $^{****}P < 0.0001$). Statistical details and replication information are described in the legend of each figure. Blots or micrographs are representative of at least three experiments that showed similar results. No statistical method was used to predetermine sample size. In the live-cell application of the as-designed biosensors, cells with overexposure were excluded from analyses. No data were excluded for other analyses. Animals or cells were randomly assigned into experimental or control groups. The investigators were not blinded to allocation during experiments and outcome assessment.

Reporting summary

Further information on research design is available in the Nature Portfolio Reporting Summary linked to this article.

Data availability

All data supporting the findings of this study are presented within the article and Supplementary files. The initial and final configurations of DHOR for molecular dynamics simulations are available in Supplementary Data 2. The protein sequence of DHOR is presented in Supplementary Fig. 9c. DNA sequences of sensors developed in this study are available in Supplementary Data 3. The LC-MS/MS data and raw files of images in this study are available on Figshare [https://doi.org/10.6084/m9.figshare.29553365][77]. Source data are provided in this paper.

References

1. Ye, D., Guan, K. L. & Xiong, Y. Metabolism, activity, and targeting of D- and L-2-hydroxyglutarates. *Trends Cancer* **4**, 151–165 (2018).
2. Dang, L. & Su, S. M. Isocitrate dehydrogenase mutation and (*R*)–2-hydroxyglutarate: from basic discovery to therapeutics development. *Annu. Rev. Biochem.* **86**, 305–331 (2017).
3. Kranendijk, M., Struys, E. A., Salomons, G. S., Van der Knaap, M. S. & Jakobs, C. Progress in understanding 2-hydroxyglutaric acidurias. *J. Inherit. Metab. Dis.* **35**, 571–587 (2012).
4. Choi, C. et al. 2-Hydroxyglutarate detection by magnetic resonance spectroscopy in IDH-mutated patients with gliomas. *Nat. Med.* **18**, 624–629 (2012).
5. Dang, L., Jin, S. & Su, S. M. IDH mutations in glioma and acute myeloid leukemia. *Trends Mol. Med.* **16**, 387–397 (2010).
6. Fathi, A. T. et al. Isocitrate dehydrogenase 1 (IDH1) mutation in breast adenocarcinoma is associated with elevated levels of serum and urine 2-hydroxyglutarate. *Oncologist* **19**, 602–607 (2014).
7. Yuan, B. F. Quantitative analysis of oncometabolite 2-hydroxyglutarate. *Adv. Exp. Med. Biol.* **1280**, 161–172 (2021).
8. Bunse, L. et al. Suppression of antitumor T cell immunity by the oncometabolite (*R*)–2-hydroxyglutarate. *Nat. Med.* **24**, 1192–1203 (2018).
9. Notarangelo, G. et al. Oncometabolite D-2HG alters T cell metabolism to impair $CD8^+$ T cell function. *Science* **377**, 1519–1529 (2022).
10. Liu, Y. et al. Metabolic functions of misunderstood D-2-hydroxyglutarate. *Innov. Life* **2**, 100101 (2024).
11. Zhang, W. et al. Coupling between D-3-phosphoglycerate dehydrogenase and D-2-hydroxyglutarate dehydrogenase drives bacterial L-serine synthesis. *Proc. Natl. Acad. Sci. USA* **114**, E7574–E7582 (2017).
12. Choe, M. & Titov, D. V. Genetically encoded tools for measuring and manipulating metabolism. *Nat. Chem. Biol.* **18**, 451–460 (2022).
13. Zhang, X. et al. FÖrster resonance energy transfer (FRET)-based biosensors for biological applications. *Biosens. Bioelectron.* **138**, 111314 (2019).
14. Zhang, Z., Cheng, X., Zhao, Y. & Yang, Y. Lighting up live-cell and in vivo central carbon metabolism with genetically encoded fluorescent sensors. *Annu. Rev. Anal. Chem.* **13**, 293–314 (2020).
15. Samsonov, V. V. et al. Revealing a new family of D-2-hydroxyglutarate dehydrogenases in *Escherichia coli* and *Pantoea ananatis* encoded by *ydiJ*. *Microorganisms* **10**, 1766 (2022).
16. Xiao, D. et al. A D-2-hydroxyglutarate biosensor based on specific transcriptional regulator DhdR. *Nat. Commun.* **12**, 7108 (2021).
17. Yang, J., Zhu, H., Zhang, T. & Ding, J. Structure, substrate specificity, and catalytic mechanism of human D-2-HGDH and insights into pathogenicity of disease-associated mutations. *Cell Discov.* **7**, 3 (2021).
18. Engqvist, M., Drincovich, M. F., Flügge, U. I. & Maurino, V. G. Two D-2-hydroxy-acid dehydrogenases in *Arabidopsis thaliana* with catalytic capacities to participate in the last reactions of the methylglyoxal and β-oxidation pathways. *J. Biol. Chem.* **37**, 25026–25037 (2009).
19. Becker-Kettern, J. et al. *Saccharomyces cerevisiae* forms D-2-hydroxyglutarate and couples its degradation to D-lactate formation via a cytosolic transhydrogenase. *J. Biol. Chem.* **291**, 6036–6058 (2016).
20. Thompson, M. G. et al. Massively parallel fitness profiling reveals multiple novel enzymes in *Pseudomonas putida* lysine metabolism. *mBio* **10**, e02577–18 (2019).
21. Davies, D. G. et al. The involvement of cell-to-cell signals in the development of a bacterial biofilm. *Science* **280**, 295–298 (1998).
22. Kang, Z. et al. An ultrasensitive biosensor for probing subcellular distribution and mitochondrial transport of L-2-hydroxyglutarate. *Adv. Sci.* **11**, e2404119 (2024).
23. Chen, Y. et al. Structural insight into enhanced calcium indicator GCaMP3 and GCaMPJ to promote further improvement. *Protein Cell* **4**, 299–309 (2013).
24. Akerboom, J. et al. Crystal structures of the GCaMP calcium sensor reveal the mechanism of fluorescence signal change and aid rational design. *J. Biol. Chem.* **284**, 6455–6464 (2009).
25. Wang, L. et al. A high-performance genetically encoded fluorescent indicator for in vivo cAMP imaging. *Nat. Commun.* **13**, 5363 (2022).
26. Li, X. et al. Ultrasensitive sensors reveal the spatiotemporal landscape of lactate metabolism in physiology and disease. *Cell Metab.* **35**, 200–211 (2023).
27. Parks, S. K., Mueller-Klieser, W. & Jacques Pouysségur Lactate and acidity in the cancer microenvironment. *Annu. Rev. Cancer Biol.* **4**, 141–158 (2020).

28. Kruse, O., Grunnet, N. & Barfod, C. Blood lactate as a predictor for in-hospital mortality in patients admitted acutely to hospital: a systematic review. *Scand. J. Trauma. Resusc. Emerg. Med.* **19**, 74 (2011).
29. Brandt, R. B., Siegel, S. A., Waters, M. G. & Bloch, M. H. Spectrophotometric assay for D-(-)-lactate in plasma. *Anal. Biochem.* **102**, 39–46 (1980).
30. Li, R. et al. Lighting up arginine metabolism reveals its functional diversity in physiology and pathology. *Cell Metab.* **37**, 1–14 (2024).
31. Fathi, A. T. et al. Elevation of urinary 2-hydroxyglutarate in IDH-mutant glioma. *Oncologist* **21**, 214–219 (2016).
32. Brunner, A. M. et al. Isocitrate dehydrogenase 1 and 2 mutations, 2-hydroxyglutarate levels, and response to standard chemotherapy for patients with newly diagnosed acute myeloid leukemia. *Cancer* **125**, 541–549 (2019).
33. Horbinski, C., Berger, T., Packer, R. J. & Wen, P. Y. Clinical implications of the 2021 edition of the WHO classification of central nervous system tumours. *Nat. Rev. Neurol.* **18**, 515–529 (2022).
34. Hua, W. et al. Rapid detection of IDH mutations in gliomas by intraoperative mass spectrometry. *Proc. Natl. Acad. Sci. USA* **121**, e2318843121 (2024).
35. Zhang, W. et al. A biosensor for D-2-hydroxyglutarate in frozen sections and intraoperative assessment of IDH mutation status. *Biosens. Bioelectron.* **247**, 115921 (2024).
36. Grant, G. A. Elucidation of a self-sustaining cycle in *Escherichia coli* L-Serine biosynthesis that results in the conservation of the coenzyme, NAD^+. *Biochemistry* **57**, 1798–1806 (2018).
37. Cai, W., Cai, X., Yang, Y., Yan, S. & Zhang, H. Transcriptional control of dual transporters involved in α-ketoglutarate utilization reveals their distinct roles in uropathogenic *Escherichia coli*. *Front. Microbiol.* **8**, 275 (2017).
38. Han, T., Kim, G. B. & Lee, S. Y. Glutaric acid production by systems metabolic engineering of an L-lysine-overproducing *Corynebacterium glutamicum*. *Proc. Natl. Acad. Sci. USA* **117**, 30328–30334 (2020).
39. Beauprez, J. J. et al. Influence of C_4-dicarboxylic acid transporters on succinate production. *Green Chem.* **13**, 2179–2186 (2011).
40. Prell, C., Burgardt, A., Meyer, F. & Wendisch, V. F. Fermentative production of L-2-hydroxyglutarate by engineered *Corynebacterium glutamicum* via pathway extension of L-lysine biosynthesis. *Front. Bioeng. Biotechnol.* **8**, 630476 (2021).
41. Nan, A. & Feher, I. C. A new polyester based on allyl α-hydroxy glutarate as shell for magnetite nanoparticles. *AIP Conf. Proc.* **1917**, 040003 (2017).
42. Martins, B. M., Macedo-Ribeiro, S., Bresser, J., Buckel, W. & Messerschmidt, A. Structural basis for stereo-specific catalysis in NAD^+-dependent (*R*)–2-hydroxyglutarate dehydrogenase from *Acidaminococcus fermentans*. *FEBS J.* **272**, 269–281 (2005).
43. Kataoka, N., Matsushita, K. & Yakushi, T. Development of a 2-hydroxyglutarate production system by *Corynebacterium glutamicum*. *Appl. Microbiol. Biotechnol.* **107**, 5987–5997 (2023).
44. Oldham, W. M., Clish, C. B., Yang, Y. & Loscalzo, J. Hypoxia-mediated increases in L-2-hydroxyglutarate coordinate the metabolic response to reductive stress. *Cell Metab.* **22**, 291–303 (2015).
45. Dang, L. et al. Cancer-associated IDH1 mutations produce 2-hydroxyglutarate. *Nature* **462**, 739–744 (2009).
46. Rohle, D. et al. An inhibitor of mutant IDH1 delays growth and promotes differentiation of glioma cells. *Science* **340**, 626–630 (2013).
47. Okoye-Okafor, U. C. et al. New IDH1 mutant inhibitors for treatment of acute myeloid leukemia. *Nat. Chem. Biol.* **11**, 878–886 (2015).
48. Wang, F. et al. Targeted inhibition of mutant IDH2 in leukemia cells induces cellular differentiation. *Science* **340**, 622–626 (2013).
49. Friedrich, M. et al. Tryptophan metabolism drives dynamic immunosuppressive myeloid states in IDH-mutant gliomas. *Nat. Cancer* **2**, 723–740 (2021).
50. Wang, X. et al. SLC1A1-mediated cellular and mitochondrial influx of R-2-hydroxyglutarate in vascular endothelial cells promotes tumor angiogenesis in IDH1-mutant solid tumors. *Cell Res.* **32**, 638–658 (2022).
51. Yee, S. W. & Giacomini, K. M. Emerging roles of the human solute carrier 22 family. *Drug Metab. Dispos.* **50**, 1193–1210 (2021).
52. Nigam, S. K. The SLC22 transporter family: A paradigm for the impact of drug transporters on metabolic pathways, signaling, and disease. *Annu. Rev. Pharmacol. Toxicol.* **58**, 663–687 (2018).
53. Koepsell, H. The SLC22 family with transporters of organic cations, anions and zwitterions. *Mol. Asp. Med.* **34**, 413–435 (2013).
54. Shinoda, Y., Yamashiro, T., Hosooka, A., Yasujima, T. & Yuasa, H. Functional characterization of human organic anion transporter 10 (OAT10/SLC22A13) as an orotate transporter. *Drug Metab. Pharmacokinet.* **43**, 100443 (2022).
55. Yee, S. W. et al. Unraveling the functional role of the orphan solute carrier, SLC22A24 in the transport of steroid conjugates through metabolomic and genome-wide association studies. *PLoS Genet.* **15**, e1008208 (2019).
56. Balss, J. et al. Enzymatic assay for quantitative analysis of (D)–2-hydroxyglutarate. *Acta Neuropathol.* **124**, 883–891 (2012).
57. Sanai, N. & Berger, M. S. Surgical oncology for gliomas: the state of the art. *Nat. Rev. Clin. Oncol.* **15**, 112–125 (2018).
58. Xiao, D. et al. A Förster resonance energy transfer-based D-2-hydroxyglutarate biosensor. *Sens. Actuators B* **385**, 133681 (2023).
59. Choate, K. A. et al. A genetically encoded fluorescent sensor enables sensitive and specific detection of IDH mutant associated oncometabolite D-2-hydroxyglutarate. *BMC Cancer* **25**, 473 (2025).
60. Okabe, M. et al. Profiling SLCO and SLC22 genes in the NCI-60 cancer cell lines to identify drug uptake transporters. *Mol. Cancer Ther.* **7**, 3081–3091 (2008).
61. Depil, S., Duchateau, P., Grupp, S. A., Mufti, G. & Poirot, L. 'Off-the-shelf' allogeneic CAR T cells: development and challenges. *Nat. Rev. Drug. Discov.* **19**, 185–199 (2020).
62. Yang, Q. et al. D2HGDH-mediated D2HG catabolism enhances the anti-tumor activities of CAR-T cells in an immunosuppressive microenvironment. *Mol. Ther.* **30**, 1188–1200 (2022).
63. Jiang, T. et al. A bacterial multidomain NAD-independent D-lactate dehydrogenase utilizes flavin adenine dinucleotide and Fe-S clusters as cofactors and quinone as an electron acceptor for D-lactate oxidization. *J. Bacteriol.* **199**, e00342–17 (2017).
64. Baginsky, M. L. & Rodwell, V. W. Metabolism of pipecolic acid in a *Pseudomonas* species IV. Electron transport particle of *Pseudomonas putida*. *J. Bacteriol.* **92**, 424–432 (1966).
65. Schäfer, A. et al. Small mobilizable multi-purpose cloning vectors derived from the *Escherichia coli* plasmids pK18 and pK19: selection of defined deletions in the chromosome of *Corynebacterium glutamicum*. *Gene* **145**, 69–73 (1994).
66. Datsenko, K. A. & Wanner, B. L. One-step inactivation of chromosomal genes in *Escherichia coli* K-12 using PCR products. *Proc. Natl. Acad. Sci. USA* **97**, 6640–6645 (2000).
67. Li, Q. et al. A modified pCas/pTargetF system for CRISPR-Cas9-assisted genome editing in *Escherichia coli*. *Acta Biochim. Biophys. Sin.* **53**, 620–627 (2021).
68. Waldo, G. S., Standish, B. M., Berendzen, J. & Terwilliger, T. C. Rapid protein-folding assay using green fluorescent protein. *Nat. Biotechnol.* **17**, 691–695 (1999).
69. Wang, Y., Cen, X. F., Zhao, G. P. & Wang, J. Characterization of a new GlnR binding box in the promoter of *amtB* in *Streptomyces coelicolor* inferred a PhoP/GlnR competitive binding mechanism for transcriptional regulation of *amtB*. *J. Bacteriol.* **194**, 5237–5244 (2012).
70. Xia, Y. et al. T5 exonuclease-dependent assembly offers a low-cost method for efficient cloning and site-directed mutagenesis. *Nucleic Acids Res.* **47**, e15 (2019).

71. Abramson, J. et al. Accurate structure prediction of biomolecular interactions with AlphaFold 3. *Nature* **630**, 493–500 (2024).
72. Fährrolfes, R. et al. ProteinsPlus: a web portal for structure analysis of macromolecules. *Nucleic Acids Res.* **45**, W337–W343 (2017).
73. Volkamer, A., Kuhn, D., Grombacher, T., Rippmann, F. & Rarey, M. Combining global and local measures for structure-based druggability predictions. *J. Chem. Inf. Model.* **52**, 360–372 (2012).
74. Chovancova, E. et al. CAVER 3.0: a tool for the analysis of transport pathways in dynamic protein structures. *PLoS Comput. Biol.* **8**, e1002708 (2012).
75. Meng, E. C. et al. UCSF ChimeraX: Tools for structure building and analysis. *Protein Sci.* **32**, e4792 (2023).
76. Schindelin, J. et al. Fiji: an open-source platform for biological-image analysis. *Nat. Methods* **9**, 676–682 (2012).
77. Liu, Y. et al. Data for a genetically encoded biosensor for point-of-care and live-cell detection of D-2-hydroxyglutarate. *Figshare* https://doi.org/10.6084/m9.figshare.29553365 (2025).

Acknowledgements

This work was supported by the grant of National Natural Science Foundation of China 32170112 (C.M.) and 32271476 (W.Z.), China Postdoctoral Science Foundation 2024M751800 (Y.L.) and 2023M742085 (Z.K.), Postdoctoral Innovation Program of Shandong Province SDCX-ZG-202400150 (Y.L.), Qingdao Postdoctoral Research Project QDBSH20230201011 (Y.L.), Youth Program of National Natural Science Foundation of China 32300029 (Z.K.), Youth Program of Natural Science Foundation of Shandong Province ZR2023QC237 (Z.K.), Youth Program of Natural Science Foundation of Qingdao City 23-2-1-31-zyyd-jch (Z.K.), Youth Program of National Natural Science Foundation of China 32400088 (D.X.), the Xi'an Science and Technology Plan Project 24YXYJ0134 (D.X.). We thank BioRender (www.biorender.com) for providing items for drawing scheme graphs. We also thank Dr. Jing Zhu, Dr. Jingyao Qu, Dr. Zhifeng Li, and Dr. Guannan Lin of the Core Facilities for Life and Environmental Sciences, State Key laboratory of Microbial Technology of Shandong University for assistance in mass spectrographic analysis; Dr. Haiyan Yu, Dr. Yuyu Guo, Dr. Xiaomin Zhao, and Dr. Sen Wang of the Core Facilities for Life and Environmental Sciences, State Key laboratory of Microbial Technology of Shandong University for assistance in confocal imaging.

Author contributions

Conceptualization: C.G., P.X., C.M., C.L., and Y.L.; Methodology: Y.L. and Z.K.; Investigation: Y.L., Z.K., R.X., S.H., L.Gong, L.Guo, K.G., X.X., X.T., D.X., and W.Z.; Animal resources: W.Z.; Clinical sample collection: G.W., S.O., J.H., and J.L.; Visualization: Y.L.; Supervision: C.G., P.X., C.M., and C.L.; Writing—original draft: Y.L. and Z.K.; Writing—review & editing: C.G., P.X., and C.M.

Competing interests

C.G., Y.L., Z.K., R.X., C.L., C.M., and P.X. have submitted a patent application to the China National Intellectual Property Administration pertaining to the development and application of the biosensor reported in this work (application number 2024104094355). The remaining authors declare no competing interests.

Additional information

Supplementary information The online version contains supplementary material available at https://doi.org/10.1038/s41467-025-62225-8.

Correspondence and requests for materials should be addressed to Chao Gao.

Peer review information *Nature Communications* thanks the anonymous reviewers for their contribution to the peer review of this work. A peer review file is available.